Downloaded from genome.cshlp.org on November 17, 2026 . Published by Cold Spring Harbor Laboratory Press



Shared transcriptional consequences of epigenetic machinery disruption in murine neuronal progenitors

Juan Ouyang, Kaan Okay, Katrín Möller, et al.

Genome Res. published online October 7, 2026
Access the most recent version at doi:10.1101/gr.281473.125

P<P Published online October 7, 2026 in advance of the print journal.

Open Access Freely available online through the *Genome Research* Open Access option.

Creative Commons License This article, published in *Genome Research*, is available under a Creative Commons License (Attribution-NonCommercial 4.0 International), as described at http://creativecommons.org/licenses/by-nc/4.0/.

Email Alerting Service Receive free email alerts when new articles cite this article - sign up in the box at the top right corner of the article or **click here.**



To subscribe to *Genome Research* go to:
https://genome.cshlp.org/subscriptions

© 2026 Ouyang et al.; Published by Cold Spring Harbor Laboratory Press

Downloaded from genome.cshlp.org on November 17, 2026 . Published by Cold Spring Harbor Laboratory Press

Research

Shared transcriptional consequences of epigenetic machinery disruption in murine neuronal progenitors

Juan Ouyang,[1,7,8] Kaan Okay,[1,7] Katrín Möller,[1,7] Katrín Wang,[1] Adam Davidovich,[2,3] Stefán Pétursson,[1] Tessa Pierce,[1,4] Arsalan Amirfallah,[1,9] Kimberley J. Anderson,[1,5,10] Kasper D. Hansen,[2,3,6] and Hans Tomas Bjornsson[1,5,6]

[1]*Louma G. Laboratory of Epigenetic Research, Faculty of Medicine, University of Iceland, 102 Reykjavik, Iceland;* [2]*Department of Biostatistics, Johns Hopkins Bloomberg School of Public Health, Baltimore, Maryland 21205, USA;* [3]*Department of Biomedical Engineering, Johns Hopkins University School of Medicine, Baltimore, Maryland 21205, USA;* [4]*California Institute of Technology, Pasadena, California 91125, USA;* [5]*Department of Genetics and Molecular Medicine, Landspitali University Hospital, 105 Reykjavik, Iceland;* [6]*Department of Genetic Medicine, Johns Hopkins University School of Medicine, Baltimore, Maryland 21205, USA*

The Mendelian disorders of the epigenetic machinery (MDEMs) are an emerging group of disorders that commonly involve disruption of intellect and growth. To investigate consequences of epigenetic machinery (EM) disruption during neurodevelopment, we systematically knocked out (KO) EM factors in neuronal progenitors isolated from the murine hippocampus and established a neurodifferentiation model to interrogate their functions. We then profile gene expression and DNA methylation (DNAm) in the EM-KOs using RNA sequencing and Nanopore long-read DNA sequencing. Although *Dnmt1*-KO induces extensive DNAm alterations, *Kmt2a*-KO has little effect on methylation. Nevertheless, the disruption of *Kmt2a* and *Dnmt1* produces convergent transcriptional changes. Loss of either EM factor leads to premature neuronal differentiation, partially explaining this convergence, and MYC emerges as a shared regulatory node linked to the downregulation of cell-cycle programs in these cells. Extending our methylation analysis to 46 EM genes, we find that loss of DNA methyltransferases induces the strongest DNAm changes, whereas other EM-KOs have subtle or negligible effects. However, clustering of EM-KOs based on promoter DNAm levels reveals three distinct EM subgroups, of which two are enriched for interactions with the DNAm machinery. Allele-specific analysis of DNAm further identifies a single differentially methylated region shared across the 46 EM-KOs, localized to the B6J allele over the *Zic4* 3′ UTR. Furthermore, *Zic4* overexpression appears to maintain the neuronal progenitor state, suggesting functional relevance of this locus. Taken together, our results reveal both gene-specific and convergent transcriptional effects across diverse EM-KOs and provide novel insights into the downstream consequences of EM dysfunction.

[Supplemental material is available for this article.]

In the past 15 years, clinicians have witnessed the rapid discovery of a group of at least 90 distinct disorders, caused mainly by heterozygous variants in the components that directly maintain the epigenome. This group of disorders is described by different names, including the Mendelian disorders of the epigenetic machinery (MDEMs) (Bjornsson 2015), chromatinopathies (Ciptasari and van Bokhoven 2020), or rare diseases of epigenetic origin (Fu et al. 2023). Despite this multitude of names, all parties agree that the disruption of these genes is likely to lead to secondary epigenetic dysregulation. Although these genes have been associated with broad phenotypic presentations (Bjornsson 2015), they also exhibit unifying disease phenotypes such as intellectual disability and growth abnormalities (Bjornsson 2015), which are present in the vast majority of patients. We have previously hypothesized that these shared phenotypic abnormalities may be caused by shared epigenetic disruption. In support of this hypothesis, we have identified common signatures of epigenetic dysregulation in three such MDEMs (Kabuki syndrome 1 & 2 and Rubinstein–Taybi syndrome): identified in blood cells for all three (Luperchio et al. 2021) and in neurons for the first two (Boukas et al. 2024).

Model systems have been central to defining how disruption of chromatin regulators affects neurodevelopment. Patient-derived and genome-edited induced pluripotent stem cells (iPSCs), neural progenitor cells, differentiated neurons, cerebral organoids, and mouse models have been used to study chromatinopathies and related neurodevelopmental disorders (Villa et al. 2022; Wang et al. 2022; Astorkia et al. 2024; Reynisdottir et al. 2025). These studies show that epigenetic dysregulation can alter developmental transcription programs, neuronal maturation, and neuronal function. In particular, DNMT1 and KMT2A have established roles in neural development: DNMT1 disruption affects neurogenesis, hippocampal development, and neuronal activity, whereas KMT2A/MLL1 regulates postnatal neurogenesis, neural progenitor proliferation, synaptic plasticity, and behavior (Feng et al. 2010; Jakovcevski et al. 2015; Jönsson et al. 2019; Bachmann et al. 2021). These prior models provide the value of

[7]These authors contributed equally to this work.
Present addresses: [8]Department of Biology, Emory University, Atlanta, GA 30322, USA; [9]The Blood Bank, Landspitali University Hospital, 103 Reykjavik, Iceland; [10]University of Akureyri, 600 Akureyri, Iceland
Corresponding authors: htb@hi.is, khansen@jhsph.edu

Article published online before print. Article, supplemental material, and publication date are at https://www.genome.org/cgi/doi/10.1101/gr.281473.125. Freely available online through the *Genome Research* Open Access option.

© 2026 Ouyang et al. This article, published in *Genome Research*, is available under a Creative Commons License (Attribution-NonCommercial 4.0 International), as described at http://creativecommons.org/licenses/by-nc/4.0/.

Downloaded from genome.cshlp.org on November 17, 2026 . Published by Cold Spring Harbor Laboratory Press

disease-relevant neural models, while underscoring the need for systematic comparisons across many epigenetic machinery genes in a controlled cellular context.

Another defining feature of these disorders is that many of them (42) exhibit distinct blood cell DNA methylation (DNAm) episignatures with diagnostic utility (Aref-Eshghi et al. 2020). Although blood may not always be the most disease-relevant tissue, many of these disorders have shared epigenetic abnormalities (Aref-Eshghi et al. 2018). Here, we have investigated whether such DNAm changes can be found in disease-relevant cells, such as neurons, and whether they can point to underlying shared pathogenic mechanisms in these disorders (Feng et al. 2013; Park et al. 2014; Zhang et al. 2014; You et al. 2015; Noguchi et al. 2016; Zhou et al. 2016; Syal et al. 2018; Carosso et al. 2019; Schoof et al. 2019; Sheu et al. 2019). Previously, multiple EM models, including those affecting KMT2D, CREBBP, and EZH2 and several others (Feng et al. 2013; Park et al. 2014; Zhang et al. 2014; You et al. 2015; Noguchi et al. 2016; Zhou et al. 2016; Syal et al. 2018; Carosso et al. 2019; Schoof et al. 2019; Sheu et al. 2019), have shown disruption of various aspects of hippocampal neurogenesis in gene-specific studies. Given this literature, we have chosen to use a hippocampal neuronal model to evaluate similarities and differences in a single context.

Recent advances in Oxford Nanopore Technologies (ONT) long-read direct DNA sequencing allow for the analysis of DNAm genome-wide and further enable haplotype phasing for the identification of allele-specific effects on DNAm (Gigante et al. 2019). Here, we applied ONT sequencing to systematically profile DNAm alterations across 46 EM knockouts (KOs) in a single disease-relevant cell-type context, murine neuronal progenitor cells (mNPCs). Among these, we examined the DNA methyltransferase DNMT1, the main maintenance methyltransferase, and the histone methyltransferase KMT2A, a regulator of H3K4 methylation associated with the neurodevelopmental disorder Wiedemann–Steiner syndrome.

Results

Systematic KO of EM factors in a single neuronal system

To comprehensively study the role of DNAm abnormalities in EM-deficient neurons, we utilized CRISPR-Cas9 technology to generate homozygous KO of EM genes in mNPCs. To obtain homogenous and efficient CRISPR-based gene KOs, we used F_1 offspring from two fully sequenced inbred mouse strains (C57BL/6J and FVB), both expressing the transgenic Cas9-GFP protein from the ROSA locus, a well-known epigenetic safe harbor region (Friedrich and Soriano 1991; Irion et al. 2007). We isolated hippocampal mNPCs at postnatal day 0 (P0) from this F_1 outcross and grew them in culture media that maintain the mNPC state. We verified cell identities (Supplemental Fig. S1A) prior to individual EM-KO experiments using 46 dual-guide lentiviral plasmids (Supplemental Table S1), each encoding two single-guide RNAs (sgRNAs) targeting the same gene. We also created eight sgRNA plasmids with random sequences (scramble gRNAs) (Supplemental Table S1) as controls. These guide vectors were individually packaged and transduced using lentiviral delivery into the Cas9-expressing mNPCs (Fig. 1A). Cells were selected for stable integration of a construct and, 4 days after transduction, harvested for profiling of DNAm (ONT sequencing) or gene expression (Illumina RNA-seq).

To confirm the efficiency of the KO in our system, we performed qPCR, western blot (WB), and immunofluorescence (IF) assays on individual EM-KO mNPCs. As expected, 4 days after transduction, we routinely saw a decrease in the relevant mRNA and protein levels for individual EM-KOs. As an example, we observed significant ($P<0.05$) downregulation of *Kmt2d* and *Ezh2* at the RNA level (Fig. 1B,C) as well as a significant ($P<0.05$) decrease in the protein levels of CHD1, KMT2A, DNMT1, EZH2, and KDM6A (Fig. 1D,E; Supplemental Fig. S1B–D) in each of their respective KOs.

To enable accurate and systematic estimation of CRISPR KO efficiency from ONT long-read sequencing data, we developed samCRISPR, a custom pipeline designed to leverage the unique features of this sequencing technique (Fig. 1F). When we compared samCRISPR with CRISPResso2 (Pinello et al. 2016), the gold standard for estimating KO efficiency from short-read data, it yielded fewer false-positive CRISPR events on average in the control samples (Supplemental Fig. S1E,F). Moreover, samCRISPR yielded a similar KO efficiency for each guide (Fig. 1G; Supplemental Fig. S1G,H) across 46 EM-KOs. As an example, when we ran two replicates of *Kmt2a*-KO and two relevant controls, we found almost no false positives in the control samples, whereas we detected on average 40% KO efficiency for either allele of the *Kmt2a*-KOs (Fig. 1H). Given the two-guide strategy, the KO efficiency of any given gene could be as high as 75%–80%. Both methods likely underestimate the actual KO efficiency owing to the small detection window (±1 bp around the cut site), and both WB and IF showed higher KO efficiency, that is, lower protein expression (40%–90%) in *Chd1*-, *Kmt2a*-, *Dnmt1*-, *Ezh2*- and *Kdm6a*-KOs (Fig. 1D,E; Supplemental Fig. S1B–D), supporting the notion that a fraction of the functional variants are not captured by either samCRISPR or CRISPResso2.

DNAm and transcriptional changes in *Dnmt1*-KO and *Kmt2a*-KO mNPCs

Having verified the KO efficiency of our system, we investigated if the disruption of individual EM genes in our mNPCs would result in DNAm abnormalities. As *Dnmt1* encodes the key maintenance DNA methyltransferase, we used it as a positive control for assessing the ONT sequencing approach. We performed ONT sequencing (Jain et al. 2016) on *Dnmt1*-KO and scrambled controls in biological triplicates. Differential methylation analysis revealed a global demethylation pattern in *Dnmt1*-KO cells, including 141,721 hypomethylated differentially methylated regions (DMRs; Q-value <0.05) (Fig. 2A; Supplemental Table S2) and a sole hypermethylated region in the *Zic1* gene body (Fig. 2B). This is consistent with prior studies showing that loss of DNMT1 in human NPCs causes global demethylation (Jönsson et al. 2019). *Dnmt1*-KO DMRs were enriched in 3′ UTRs, introns, and exons but were depleted in promoters, intergenic regions, and 5′ UTRs (Fig. 2C; Supplemental Table S3).

Given the extensive DNAm changes in *Dnmt1*-KO, we explored whether *Dnmt1*-KO DMRs show enrichment of TF binding motifs using an analysis of motif enrichment (AME; MEME-suite, mouse HOCOMOCO v11 core motifs). This analysis identified 177 known TF binding motifs that were significantly enriched (Fisher's exact test, adjusted P-value <0.05) (Fig. 2D; Supplemental Table S4), including a motif for MECP2, which has been shown to recruit DNMT1 to hemi-methylated or fully methylated CpGs (Kimura and Shiota 2003). However, we also found other noteworthy TF motifs, some with CpG sites in their binding motifs, such as HIF1A, AHR, and ARNT, and others lacking CpGs in their motifs, including SMAD3, ESR2, NKX2-5, and MXI1 (Fig. 2D; Supplemental Table S4). Several hypoxia-related TF motifs

Downloaded from genome.cshlp.org on November 17, 2026 . Published by Cold Spring Harbor Laboratory Press

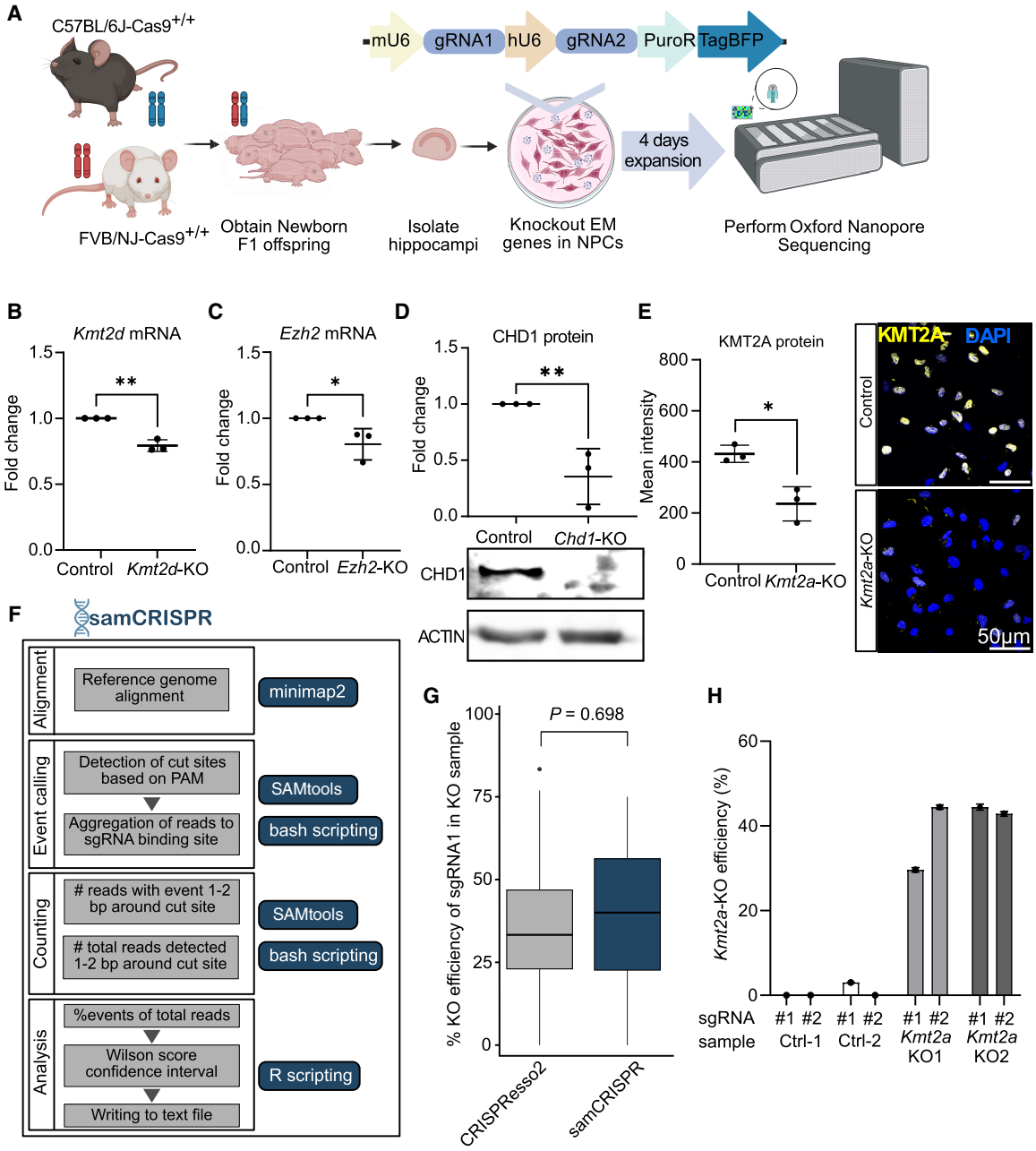


Figure 1. Effective CRISPR-Cas9 targeting in a disease-relevant cellular system. (*A*) Schematic workflow of EM-KO in mNPCs using lentiviral vectors followed by evaluation of DNAm with ONT sequencing. (*B*,*C*) Gene expression changes of *Kmt2d* ($P = 0.0013$; *B*) and *Ezh2* ($P = 0.0229$; *C*) in mNPCs after knocking out *Kmt2a* or *Ezh2* with CRISPR-Cas9 compared with a scrambled control ($n = 3$). An unpaired *t*-test was used to calculate significance. (*D*) Protein levels and quantification of CHD1 after knocking out *Chd1* with CRISPR-Cas9 compared with a scrambled control ($n = 3$, $P = 0.0054$). An unpaired *t*-test was used to calculate significance. (*E*) Quantification of KMT2A mean intensity per cell in *Kmt2a*-KO and scrambled controls ($n = 3$, $P = 0.0001$). An unpaired *t*-test was used to calculate significance. (*F*) Schematic of the samCRISPR analysis tool for KO efficiency estimation of long-read sequencing data. (*G*) KO efficiency estimates from *CRISPResso2* and samCRISPR were comparable for sgRNA1 across 46 EM-KOs from ONT WGS sequencing data (37.5% vs. 39.1%, two tailed *t*-test). (*H*) Bar plot showing *Kmt2a*-KOs efficiencies for sgRNA 1 and 2 in two *Kmt2a*-KOs and controls (Ctrl) calculated by samCRISPR. (*) $P < 0.05$, (**) $P < 0.01$, (***) $P < 0.001$, (ns) not significant.

(HIF1A, EPAS1, and ARNT) emerged. These are of particular interest given our recent observation of dysregulated hypoxia signaling in Kabuki syndrome, one of the MDEMs, caused by mutations in *KMT2D* (Carosso et al. 2019). We next asked if the enrichment of TF motifs in the *Dnmt1*-KO-associated DMRs could reflect known DNMT1 interaction partners. We compared these motifs with known DNMT1 interactors from BioGRID (Oughtred et al. 2021) and found that 13 of the 24 interactors represented in the HOCOMOCO database exhibited motif enrichment in *Dnmt1*-KO DMRs (Supplemental Fig. S2A).

To investigate whether methylation changes in *Dnmt1*-KOs coincide with changes in transcription, we performed RNA-seq

Downloaded from genome.cshlp.org on November 17, 2026 . Published by Cold Spring Harbor Laboratory Press

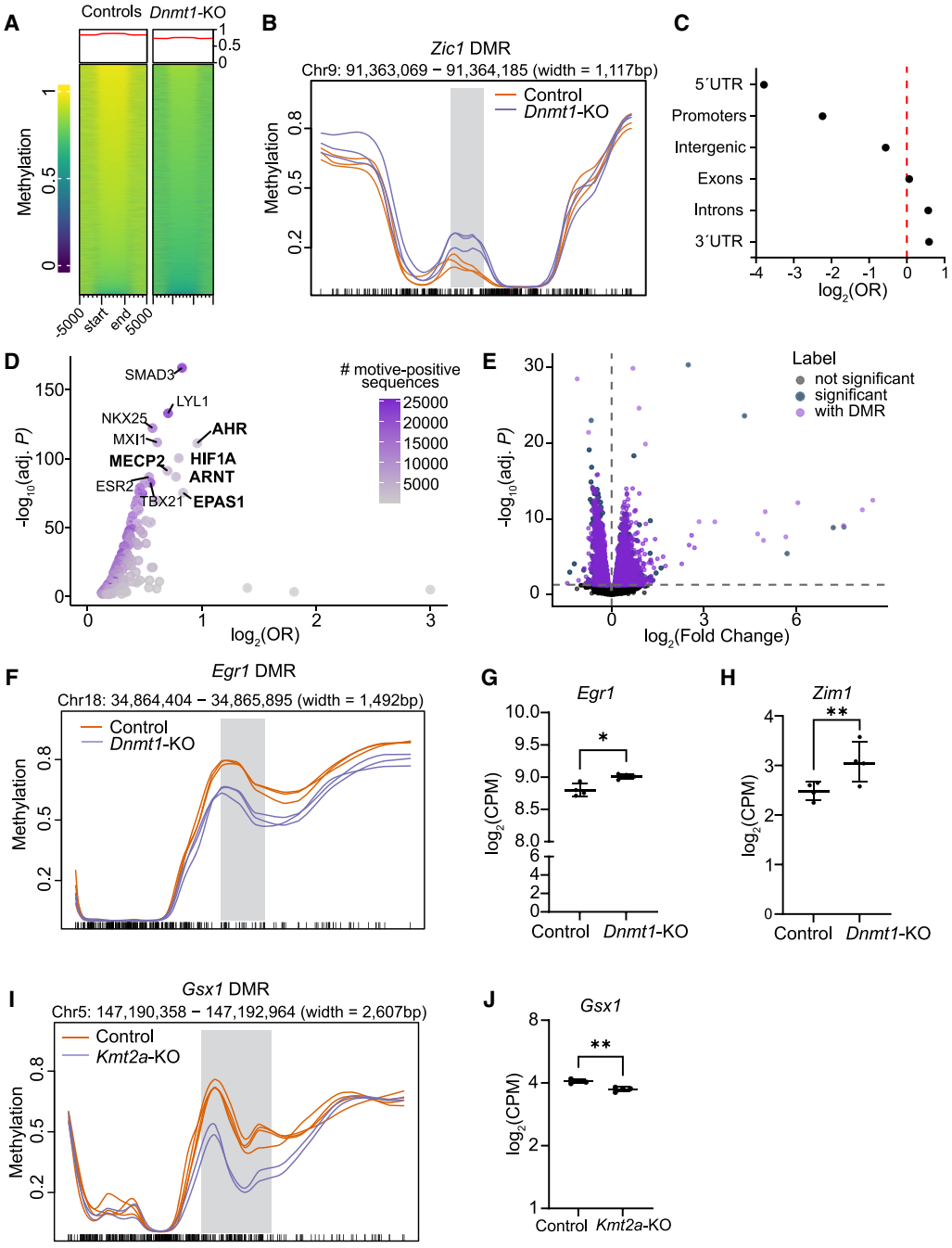


Figure 2. Extent and impact of DNA methylation (DNAm) changes in *Dnmt1*-KO and *Kmt2a*-KO mNPCs. (*A*) Enrichment heatmaps of smoothed CpG methylation across 141,722 *Dnmt1*-associated DMRs. Each horizontal line represents the average smoothed methylation profile across CpG sites within a DMR and ±5 kb flanking regions. Yellow indicates higher smoothed methylation; blue, lower smoothed methylation. (*B*) The *Zic1* DMR (*Q*-value < 0.05; gray vertical bar) in *Dnmt1*-KOs (purple) compared with control NPCs (orange). Flanking regions of DMR are ±5 kb. On the *x*-axis, each tick mark represents a CpG in the mouse genome. (*C*) The enrichment analysis of the DMR distribution in *Dnmt1*-KOs, using a Fisher's exact test. All categories are significantly enriched or depleted ($P < 0.05$). The exact value is listed in Supplemental Table S3. (*D*) Scatter plot showing enriched TF motifs in *Dnmt1*-KO DMRs (adjusted *P*-value < 0.05). (*E*) A volcano plot showing the distribution of *Dnmt1*-KO DEGs, with significant genes (adjusted *P*-value < 0.05) in dark blue and DEGs with DMRs associated in purple. (*F*) *Egr1* DMR (*Q*-value < 0.05; gray vertical bar) in *Dnmt1*-KOs (purple) compared with control NPCs (orange). Flanking regions of DMR are ±5 kb. On the *x*-axis, each tick mark represents a CpG in the mouse genome. (*G*) RNA-seq results showing normalized *Egr1* counts in *Dnmt1*-KOs compared with control NPCs. Adjusted *P*-value < 0.05. (*H*) RNA-seq results showing normalized *Zim1* counts in *Dnmt1*-KOs compared with control NPCs. Adjusted *P*-value < 0.05. (*I*) *Gsx1* DMR (*Q*-value < 0.05, gray vertical bar) found in *Kmt2a*-KO NPCs (orange) compared with control NPCs (purple). Flanking regions of DMR are ±5 kb. On the *x*-axis, each tick mark represents a CpG in the mouse genome. (*J*) RNA-seq results showing normalized *Gsx1* counts in *Kmt2a*-KOs and controls. (*) $P < 0.05$, (**) $P < 0.01$, (ns) not significant.

Downloaded from genome.cshlp.org on November 17, 2026 . Published by Cold Spring Harbor Laboratory Press

on *Dnmt1*-KO cells. Focusing on protein-coding genes, we identified 3545 differentially expressed genes (DEGs) compared with the controls (Supplemental Table S5). Using HOMER to annotate the *Dnmt1*-KO DMRs, we found that 2713 of the 3456 DEGs (78.5%) were associated with at least one DMR (Fig. 2E, purple). This proportion was significantly higher than that observed for all detected protein-coding genes (9486 out of 12,546, 75.6%; Fisher's exact test, OR = 1.25, 95% CI: 1.14–1.37, $P = 2.89 \times 10^{-6}$). Among these were *Ppfibp1* (Supplemental Fig. S2B; Wei et al. 2011); the immediate early genes *Jun*, *Fos*, and *Egr1* (Fig. 2F,G; Supplemental Fig. S2C; Kim et al. 2018; Veyrac et al. 2014); and *Rora* and *Itga8* (Supplemental Fig. S2C,D), previously identified DNMT1 targets (Tao et al. 2022). We also found that mouse imprinted genes were significantly overrepresented in the *Dnmt1*-KO associated DEGs (Fisher's exact test, OR = 1.83, $P = 0.0118$), including *Zim1* (Fig. 2H; Kim et al. 1999).

We next examined the impact of knocking out KMT2A, a histone methyltransferase that is expected to have a more indirect influence on DNAm compared with DNMT1. Nevertheless, pathogenic variants in *KMT2A* are the cause of Wiedemann–Steiner syndrome (OMIM 605130), which has a distinct DNAm signature in peripheral blood (Foroutan et al. 2022). To investigate whether *Kmt2a* loss also perturbs DNAm in neuronal progenitors, we performed ONT sequencing on *Kmt2a*-KO NPCs in duplicates, which revealed only three genome-wide significant DMRs compared with the controls. One of these DMRs was located in the 3′ UTR of the *Gsx1* gene (meanDiff = 0.0011, *Q*-value = 0.042) (Fig. 2I). We also performed RNA-seq after *Kmt2a*-KO and found 2106 DEGs compared with the controls (Supplemental Table S6). Among the previously identified DMRs, only one is associated with a gene exhibiting significant changes in gene expression, *Gsx1* (Fig. 2J). GSX1 is a TF expressed early in NPCs and is known to promote maturation in specific neuronal subtypes (Pei et al. 2011; Coltogirone et al. 2023). Notably, a prior study reported reduced H3K4me1 near this DMR in *Kmt2a* knockdown neurons derived from a mouse model (Supplemental Fig. S2E; Kerimoglu et al. 2017), supporting that *Gsx1* may be a direct target of KMT2A in mNPCs. We then queried GSX1 target genes in our *Kmt2a*-KO DEGs. Using the TFBS database, which predicts TF–target gene interactions from DNA motifs and ENCODE DNase I footprints (Plaisier et al. 2016), we identified 133 GSX1 target genes (19.2% of 693 expressed targets) that overlapped with *Kmt2a*-KO DEGs. However, this overlap was not significantly enriched (Fisher's exact test, OR = 1.18 and $P = 0.055$). To further explore whether *Gsx1* regulation might also be influenced by other EM genes, we examined the *Dnmt1*-KO. Although we identified two intergenic DMRs near (~30 kb and ~16.5 kb upstream) the *Gsx1* locus in *Dnmt1*-KO (Supplemental Fig. S2F,G), *Gsx1* did not exhibit corresponding transcriptional changes in *Dnmt1*-KO. We also noticed that GSX1 targets were modestly enriched among *Dnmt1*-KO DEGs (Fisher's exact test, OR = 1.16, $P = 0.044$).

Convergence of gene expression changes after *Dnmt1* and *Kmt2a* disruption

Given the phenotypic overlap among multiple MDEMs, we next investigated the overlap in molecular consequences between *Kmt2a*-KOs and *Dnmt1*-KOs. When we compared the DEGs from both *Dnmt1*-KO and *Kmt2a*-KO cells, we found a substantial overlap of 1542 DEGs (44.7% of *Dnmt1*-KO DEGs and 73.3% of *Kmt2a*-KO DEGs), including 682 upregulated and 860 downregulated genes (Fisher's exact test, OR = 11.6, $P < 0.0001$) (Fig. 3A; Supplemental Table S7). Moreover, gene expression changes were highly correlated between the two data sets (Spearman's $\rho = 0.94$, $P < 0.0001$) (Fig. 3B), and almost all shared DEGs were concordant in regard to the direction of change. In both data sets, the upregulated genes were enriched in neuronal differentiation and maturation GO terms (Fig. 3C), whereas the downregulated genes were enriched in GO terms linked to cell cycle and chromosome organization (Fig. 3D). We also performed a gene set enrichment analysis (GSEA) of both data sets, which revealed significant enrichment of downregulated genes in hallmark terms such as MYC and E2F targets, as well as G_2-M checkpoint pathways (FDR < 0.05) (Fig. 3E; Supplemental Fig. S3A–C), consistent with reduced proliferative activity. Although *Myc* is a master regulator of cell-cycle progression (Bretones et al. 2015), it was not differentially expressed in either data set (Supplemental Fig. S3D,E). However, many canonical MYC downstream effectors, including E2F family, cyclin genes, *Cdk1*, *Cdk2*, *Cdkn2b*, and *Cdkn1a*, showed the expected direction of change (Fig. 3F; Supplemental Fig. S3F; Bretones et al. 2015). MYC regulators such as *Usp28* and *Skp2* were also downregulated (Fig. 3F; Supplemental Fig. S3F). Given that both KMT2A and DNMT1 have reported physical interactions with MYC on BioGRID (Kalkat et al. 2018), these patterns suggest that disruption of either factor may drive cells toward cell-cycle exit and premature differentiation.

We explored the expression of other EM factors and found that 27 EM genes were differentially expressed in both data sets (Supplemental Fig. S3G), including *Ezh2*, a known barrier to neuronal differentiation (Ciceri et al. 2024), and the core DNAm factor *Dnmt1* and its key interactor *Uhrf1*, suggesting that core DNAm machinery may be disrupted in both KOs. We next asked whether the shared DEGs were driven by common regulatory programs, using motif enrichment analysis of their promoter regions. AME (MEME-suite) of promoter regions of the shared DEGs identified common TF motifs, including members of the specificity protein (SP) and E2F families, most notably SP2 and E2F4 (Fig. 3G; Supplemental Table S8), both of which are known regulators of cell-cycle progression and differentiation in neuronal cells (Persengiev et al. 1999; Liang et al. 2013). We wondered if any of these TFs could interact with both KMT2A and DNMT1, thereby possibly explaining the overlapping expression changes. By comparing known interactors that were expressed in our system for either protein from BioGRID, we found a significant overlap of 53 interactors (Fisher's exact, OR = 18.5, $P < 0.0001$) (Supplemental Fig. S3H). Five of these had enriched motifs in the shared DEGs, most notably at SP1 and E2F6 targets but also at MYC targets (Fig. 3G, boxes).

To determine whether *Kmt2a*-KO and *Dnmt1*-KO mNPCs undergo premature differentiation, we explored markers for neuronal and glial differentiation in both KOs and scrambled control mNPCs, using WB and IF staining. WB analysis revealed a significant increase in the neuronal marker TUBB3 in *Kmt2a*-KO mNPCs but not the *Dnmt1*-KO mNPCs compared with the controls (Supplemental Fig. S4A). No notable differences in the proliferation marker PCNA were detected in either KO model (Supplemental Fig. S4B). IF staining demonstrated a greater number of TUBB3-positive cells in both the *Kmt2a*-KO and *Dnmt1*-KO cultures compared with the scrambled controls, along with distinct morphological changes of the *Kmt2a*-KO TUBB3-positive cells, such as smaller cell bodies and elongated projections, indicative of differentiation (Fig. 3H,I; Supplemental Fig. S4C,D). Increased expression of the astrocyte marker EAAT2 was also observed in *Dnmt1*-KO cultures, whereas no significant change was

Downloaded from genome.cshlp.org on November 17, 2026 . Published by Cold Spring Harbor Laboratory Press

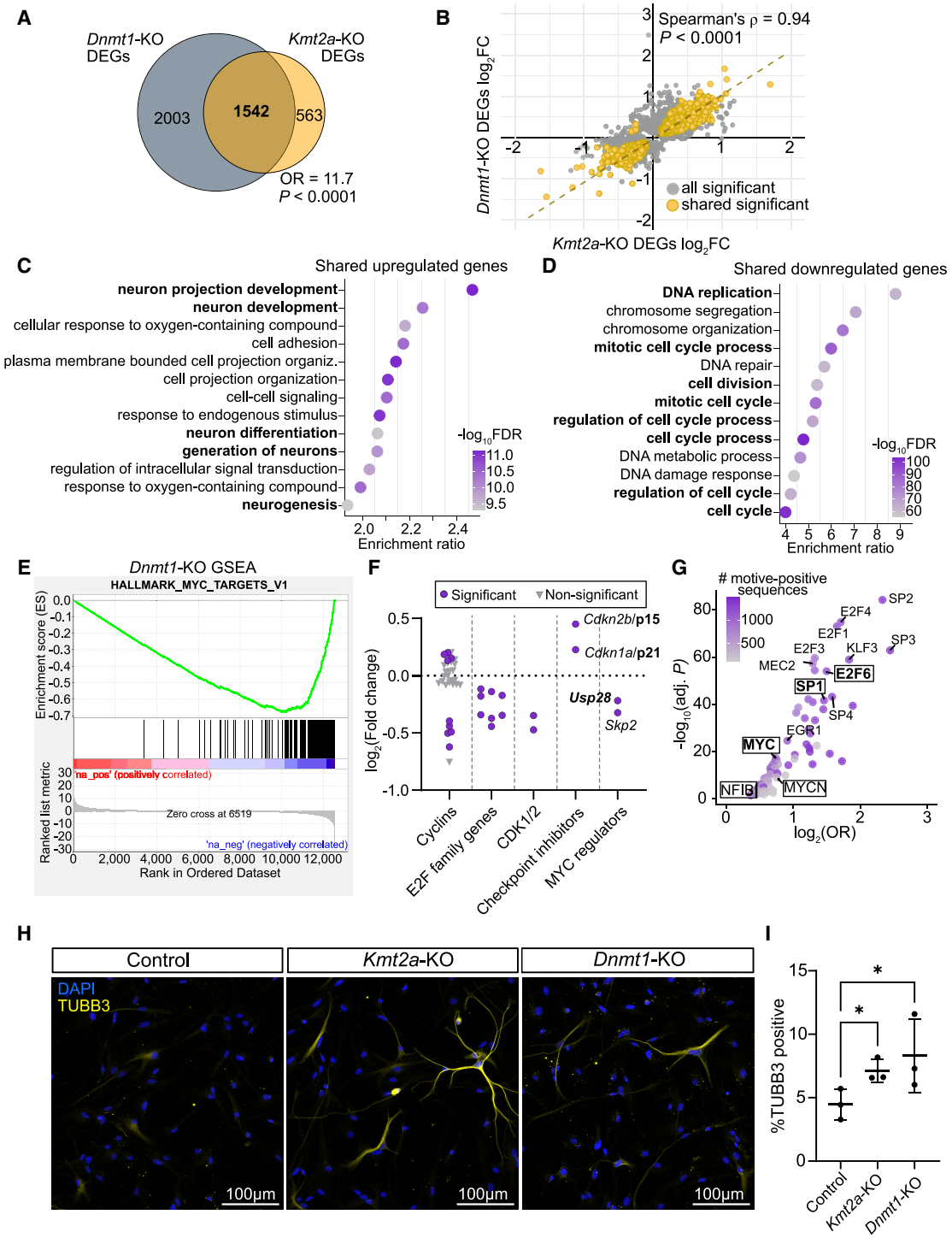


Figure 3. Premature differentiation in *Kmt2a*-KO and *Dnmt1*-KO. (*A*) Venn diagram showing extensive overlap of DEGs in *Dnmt1*-KO and *Kmt2a*-KO cells compared with control NPCs, with results from a Fisher's exact test (OR = 11.7, $P < 0.0001$). (*B*) Scatter plot showing the $\log_2$fold change (FC) of significant DEGs from both *Dnmt1*-KOs and *Kmt2a*-KOs in gray and the shared significant DEGs in yellow. Spearman's correlation was calculated for the shared DEGs ($R = 0.94$, $P < 0.0001$). (*C*) Gene Ontology (GO) term analysis (biological process) of overlapping upregulated genes, showing enrichment ratio of each GO term on the *x*-axis and color depicting the FDR. (*D*) GO term analysis (biological process) of overlapping downregulated genes showing enrichment ratio for each GO term on the *x*-axis and color depicting the FDR. (*E*) GSEA plots showing the MYC_targets_V1 hallmark category for *Dnmt1*-KO genes. (*F*) RNA-seq results showing gene expression changes in *Dnmt1*-KO NPCs compared with controls. The *y*-axis shows the $\log_2$FC of genes belonging to the categories on the *x*-axis. Purple dots show significant genes; gray triangles show nonsignificant genes. (*G*) Scatter plot of TFs ranked by the number of promoters containing their binding motifs. The odds ratio indicates the motif overrepresentation in promoters of shared DEGs. Boxes label shared BioGRID interactors. (*H*) IF staining of mNPCs after *Kmt2a*-KO and *Dnmt1*-KO compared with controls: Blue indicates DAPI; yellow, TUBB3; and magenta, EAAT2. (*I*) Quantification of the percentage of TUBB3-positive cells in *Kmt2a*-KO, *Dnmt1*-KO, and controls. A one-way ANOVA with an FDR correction was used to calculate significance. (*) $P < 0.05$.

Downloaded from genome.cshlp.org on November 17, 2026 . Published by Cold Spring Harbor Laboratory Press

detected in *Kmt2a*-KO cells (Supplemental Fig. S4E,F). Prior work has shown prematurely poised neuronal enhancers in primary mNPCs from a *Kmt2a*-haploinsufficient model, a phenotype that normalized after genetic rescue of *Kmt2a* (Reynisdottir et al. 2025). We found that NPCs from this model exhibit a similar premature neuronal differentiation phenotype as in our full KO (Supplemental Fig. S4G,H), supporting that this is a feature of *Kmt2a* disruption. These findings support that the loss of both factors contributes to premature differentiation of mNPCs but that they differ in impact. Specifically, loss of *Kmt2a* leads to a premature differentiation signature, whereas *Dnmt1* deficiency promotes both neuronal and glial differentiation but potentially in a more variable manner.

Evaluation of changes that occur during normal differentiation

Given the premature differentiation observed in EM-KOs, some of the expression changes may reflect differences in cell-state composition across genotypes. To explore the extent of this in our EM-KOs, we differentiated wild-type (WT) mNPCs into mixed neuronal cultures (see Methods) and demonstrated that these cultures express typical markers for neurons and astrocytes, as well as synaptic markers at day 6 (Supplemental Fig. S5A). We then performed RNA-seq on mNPCs and day 2 and day 6 differentiating cells (for schematic, see Fig. 4A), which yielded 3706 and 3441 DEGs at day 2 and day 6, respectively, compared with mNPCs (Supplemental Tables S9, S10), and changes were consistent with the developmental time point (Supplemental Fig. S5B). Both time points were enriched in neurogenic and synaptic terms, consistent with ongoing neural differentiation and maturation of the culture (Supplemental Fig. S5C,D). Additionally, a GSEA of cell types showed significant enrichment in cell-type markers for the three main brain-cell lineages (neurons, astrocytes, and oligodendrocytes) (Supplemental Fig. S5E), as would be expected.

To understand the extent of transcriptional changes that may be secondary to premature differentiation in *Dnmt1*-KOs and *Kmt2a*-KOs, we compared DEGs from each KO to those identified during normal neuronal differentiation (mNPCs vs. day 2 and day 6). DEGs from both KOs showed strong and consistent overlap with normal differentiation associated gene expression changes (ORs > 2 in all comparisons, $P < 0.0001$, Fisher's exact test) (Fig. 4B) and displayed a linear correlation (Spearman's $\rho > 0.45$ for all comparisons, $P < 0.0001$) (Fig. 4C–F). These results suggest substantial convergence between KO-induced and differentiation-related transcriptional programs, consistent with a premature differentiation phenotype in the previously described EM-KOs.

To map the temporal landscape of DNAm during neuronal differentiation, we profiled genome-wide DNAm using ONT in mNPCs at day 0, day 2, and day 6 of differentiation (Fig. 4A). A principal component analysis (PCA) of genome-wide DNAm showed that the developmental stage was the main driver of methylation variance, as captured by PC1 (Supplemental Fig. S5F). Differential methylation analysis identified no significant changes at day 2 compared with day 0 mNPCs, but it revealed 8627 genome-wide significant DMRs (Q-value < 0.05) at day 6 compared with day 0 mNPCs, indicating that most DNAm remodeling occurs relatively late in differentiation (Fig. 4G; Supplemental Table S11). Genome-context analysis showed that day 6 DMRs, similar to *Dnmt1*-KO DMRs, were enriched in introns, 3′ UTRs, and exons, but they were depleted in promoters, 5′ UTRs, and intergenic regions (Supplemental Fig. S5G). To assess whether the methylation dynamics observed during normal differentiation are recapitulated in the KOs, we examined the methylation state of the day 6 DMR regions in *Dnmt1*-KO and *Kmt2a*-KO cells. *Kmt2a*-KO cells maintained a methylation profile similar to that of undifferentiated mNPCs at these loci, whereas *Dnmt1*-KO cells exhibited a methylation pattern resembling that of day 2 neurons (Fig. 4H). Notably, methylation levels adjacent to these day 6 DMRs were also lower in *Dnmt1*-KO cells, suggesting that the effects are not specific to those regions but rather a global effect. Additionally, 1154 of the day 6 DMRs were also identified in *Dnmt1*-KO cells (OR = 1.48, $P < 2.2 \times 10^{-16}$) (Supplemental Table S12). This suggests that the methylation changes over these day 6 DMRs are driven by global hypomethylation in *Dnmt1*-KO cells but that they are also consistent with aspects of premature differentiation. Taken together, these results suggest that transcriptional changes in the context of EM-KO are largely independent of concurrent DNAm changes.

An expanded cohort of EM-KOs shows subtle DNAm changes

We next broadened our analysis by profiling DNAm abnormalities across 44 additional EM-KO and matched scrambled controls using ONT long-read whole-genome sequencing (WGS). These data were pooled with previously generated data from the *Dnmt1*-KO and *Kmt2a*-KO, resulting in a total of 46 EM-KOs and 16 control samples. We systematically evaluated genome-wide DNAm changes, and PCA revealed that two known DNAm machinery components, *Dnmt1* and *Dnmt3b*, showed the most DNAm abnormalities (Supplemental Fig. S6A). When these two were excluded from the analysis, *Kat6a*, *Chd5*, and *Tet1* emerged as outliers, clustering separately from the remaining EM-KOs (Supplemental Fig. S6B). Despite this variation, no shared DMRs were identified across the 46 EM-KOs.

Promoter DNAm alterations depend on interactions with the DNAm machinery

Given the diverse roles of EM genes in modulating DNAm, we hypothesized that shared DMRs may exist within specific subgroups of EM-KOs with related molecular functions. Therefore, classifying EM genes based on regional DNAm patterns could help uncover convergence. Promoter regions are well-established regulatory elements that are easily assigned to the corresponding genes and are involved in transcriptional control (Deaton and Bird 2011). To investigate whether a subset of EM-KOs exhibit similar DNAm changes at gene promoters, we applied nonnegative matrix factorization (NMF) to cluster the 46 EM-KOs based on DNAm patterns at the promoters of 20,482 mouse protein-coding genes (Supplemental Fig. S6C). Hierarchical clustering of EM-KOs using the NMF-derived coefficients of latent factors (a statistical aspect of the NMF-analysis) was used to delineate three EM clusters (Fig. 5A). Specifically, cluster 1 included *Chd3*, *Setd4*, *Setd1a*, *Setd1b*, *Kdm5b*, and *Kdm1a*, showing the highest coefficient in latent factor 3. In contrast, cluster 2 included the controls and showed low coefficients in all three latent factors. Finally, cluster 3 included the genes *Kmt2a*, *Dnmt1*, *Chd1*, *Kdm6a*, *Hdac6*, *Ezh2*, and *Crebbp* and showed the highest coefficient in latent factor 2 (Fig. 5A). *Dnmt3b*-KO showed the highest coefficient in latent factor 1 and did not cluster with other EM genes (Fig. 5A). Genes with the highest weight in latent factor 2 were significantly enriched in GO terms related to generation of neurons and neurodifferentiation (Fig. 5B) as well as the Wnt signaling pathway (Supplemental Fig. S6D). Conversely, no significant enrichment in GO terms was found for the other latent factor groups. However, separate

Downloaded from genome.cshlp.org on November 17, 2026 . Published by Cold Spring Harbor Laboratory Press

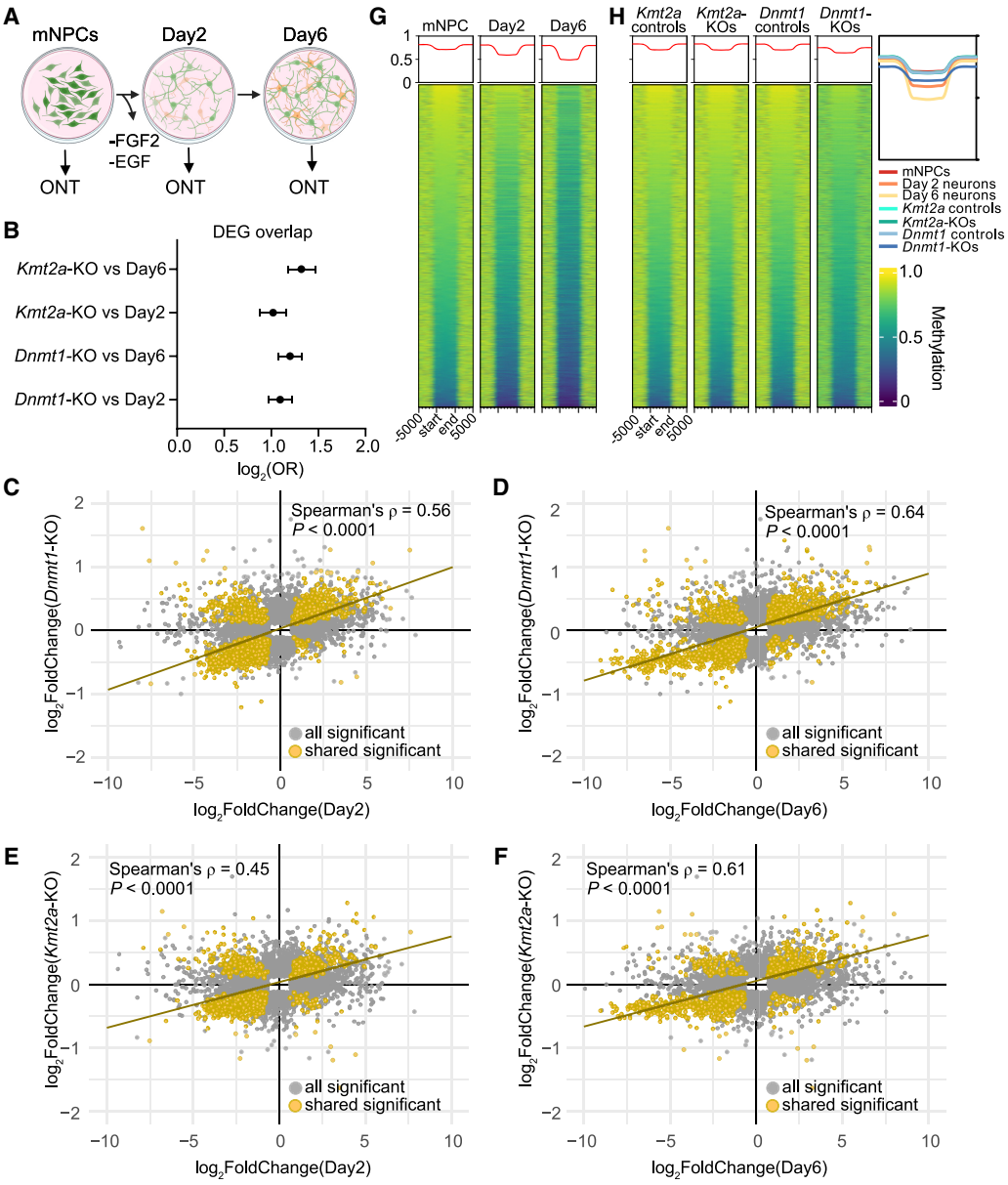


Figure 4. Changes observed in DNAm and gene expression during differentiation of NPCs. (*A*) A schematic of the neurodevelopmental model. (*B*) Odds ratio for the overlap between *Kmt2a*-KO and *Dnmt1*-KO DEGs with NPC-day 2 and NPC-day 6 DEGs, with 95% confidence intervals shown (Fisher's exact test). (*C*–*F*) Significant Spearman's correlations between DEGs of *Dnmt1*-KO versus day 2 (*C*), *Dnmt1*-KO versus day 6 (*D*), *Kmt2a*-KO versus day 2 (*E*), and *Kmt2a*-KO versus day 6 (*F*). Axis represents $\log_2$FC for each data set. (*G*) Day 6 DMRs are shown in mNPCs and day 2 and day 6 neurons. (*H*) Day 6 DMRs in KO and control samples. In the enriched heatmaps in *G* and *H*, each line demonstrates the average smoothed methylation values across all CpGs in the corresponding DMR. DMRs were aligned at the DMR start site (start) and end site (end), ±5 kb on either side. Yellow shows higher smooth methylation, and blue shows lower smooth methylation values.

DNAm analysis comparing each of these clusters to the controls did not reveal any genome-wide significant DMRs. In the two clusters that did not group with the controls (clusters 1 and 3), nearly all the gene members (excluding SETD4) had STRING-defined interactions with the maintenance methyltransferase DNMT1 (Fig. 5A). Indeed, components of these clusters had a significant enrichment in interactions with all the enzymatic DNAm machinery components (Fig. 5A,C). This enrichment was strongest for the maintenance methyltransferase (DNMT1) but less so for de novo methyltransferases (Fig. 5C). Furthermore, the same groups (clusters 1 & 3 and DNMT3B) had a significantly higher number of STRING interactions with other members of the DNAm machinery ($n = 25$) (Boukas et al. 2019) compared with what was seen in cluster 2 (one-sided Wilcoxon rank-sum test, $W = 349.5$, P-value $= 0.0014$) (Fig. 5D). This observation holds even when interactions are limited to BioGRID interactions, which are experimentally verified (one-sided Wilcoxon rank-sum test, $W = 122.5$, P-value $= 0.0062$) (Supplemental Fig. S6E). These same groups all involve factors with enzymatic activity, whereas readers of epigenetic marks are only present in cluster 2. These results suggest

Downloaded from genome.cshlp.org on November 17, 2026 . Published by Cold Spring Harbor Laboratory Press

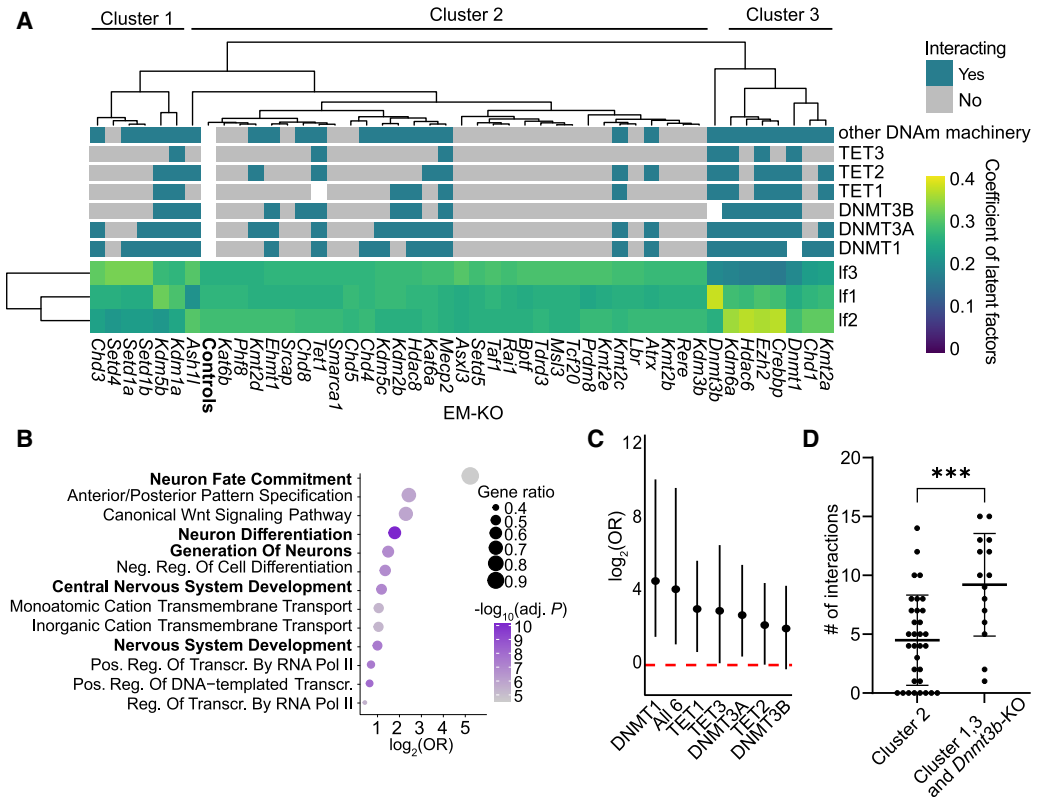


Figure 5. DNAm analysis of 46 EM-KO genes in NPCs reveals shared promoter effects. (*A*) Composite graph showing STRING interactions of EM components with enzymatic DNAm components on *top*. The heatmap shows coefficient of latent factors for each EM-KO across three latent factors. The color scale represents the coefficient of each latent factor (yellow shows a higher but blue shows a lower latent factor coefficient). (*B*) GO term enrichment (biological process) of the genes associated with latent factor 2. Size represents the ratio of genes in the relevant GO term; color indicates the $-\log_{10}$(adjusted *P*-value). (*C*) Forest plot showing enrichment of enzymatic DNAm machinery-interacting EMs in two relevant clusters compared with the rest. Significance testing was done with a Fisher's exact test. Dots represent Fisher's exact test OR ($\log_2$scale), with lines indicating 95% confidence intervals. The horizontal dotted red line represents statistical significance. (*D*) Comparison of number of STRING interactions with 25 DNAm machinery components between the clusters. A Wilcoxon rank-sum test was used for significance. (If1) Latent factor 1, (If2) latent factor 2, (If3) latent factor 3. (***) $P < 0.001$.

that enzymatic EM factors, outside the core DNAm machinery, may influence promoter DNAm through interactions with components of the DNAm machinery.

Haplotype-specific DNAm within the context of EM-KOs

We used mNPCs derived from F_1 offspring of the two strains (FVB maternal × B6J paternal) (Fig. 1A). As the B6J and FVB mouse strains differ genetically, with a single-nucleotide variation (SNV) between the two genomes roughly every 630 bp, it is possible to phase sequenced reads and perform an allele-specific methylation analysis. This is an average statistic; in practice roughly half of the two genomes can be phased. PCA of the phased data shows the same pattern between KOs and controls as for the unphased data (Supplemental Fig. S7A) but supports the presence of haplotype-specific methylation between the two strains. Indeed, within the control samples, we identified 1074 haplotype-specific DMRs (family-wise error rate [FWER] < 0.05) (Fig. 6A; Supplemental Table S13; Do et al. 2016; Tycko 2010), including one located in the exon 4 of *Tet3* (Fig. 6B). Because of the consistent parental origin of the two genomes in these F_1 crosses, imprinted loci will manifest as allele-specific methylation patterns within a single cross direction. Using 23 known ICR regions (Gigante et al. 2019), we have coverage on both haplotypes for 16 of the 23, and all 16 exhibit strong methylation differences between the two alleles (for an example, see Supplemental Fig. S7B).

To determine if the EM clusters, identified via the NMF analysis (Fig. 5A), yielded any shared haplotype-specific DMRs, we performed a grouped analysis on the phased data for each of these clusters, compared with the controls. Cluster 1 (*Chd3*, *Setd4*, *Setd1a*, *Setd1b*, *Kdm5b*, and *Kdm1a*) showed a shared hypomethylated DMR localized to the FVB allele 4.6 kb upstream of the gene *Ebf1* (FWER = 0.03) (Fig. 6C), which encodes a TF involved in early neurogenesis (Garel et al. 1999; La Manno et al. 2021). In contrast, cluster 2 and 3 did not yield any shared DMRs compared with the controls. Finally, we searched for haplotype-specific DMRs associated with the entire group of 46 EM-KOs and identified a single shared hypomethylated DMR localized to the B6J allele (FWER < 0.05). This DMR is located in the 3′ UTR of *Zic4* (Fig. 6D; Supplemental Fig. S7C), which encodes a TF that plays a role in cerebellar development (Grinberg et al. 2004). Studies using DNAm arrays in humans have shown that (1) the 3′ UTR of this gene is dynamically methylated during differentiation from hESCs to neurons (Samara et al. 2022) and (2) methylation of the gene body contributes to an episignature for Sotos syndrome (Choufani et al. 2015). Although *Zic4* was not differentially expressed in either *Dnmt1*-KO and *Kmt2a*-KO mNPCs compared with the scrambled controls (Supplemental Fig. S7D,E), it was significantly downregulated ($\log_2$FC = −1.978, adjusted *P*-

Downloaded from genome.cshlp.org on November 17, 2026 . Published by Cold Spring Harbor Laboratory Press

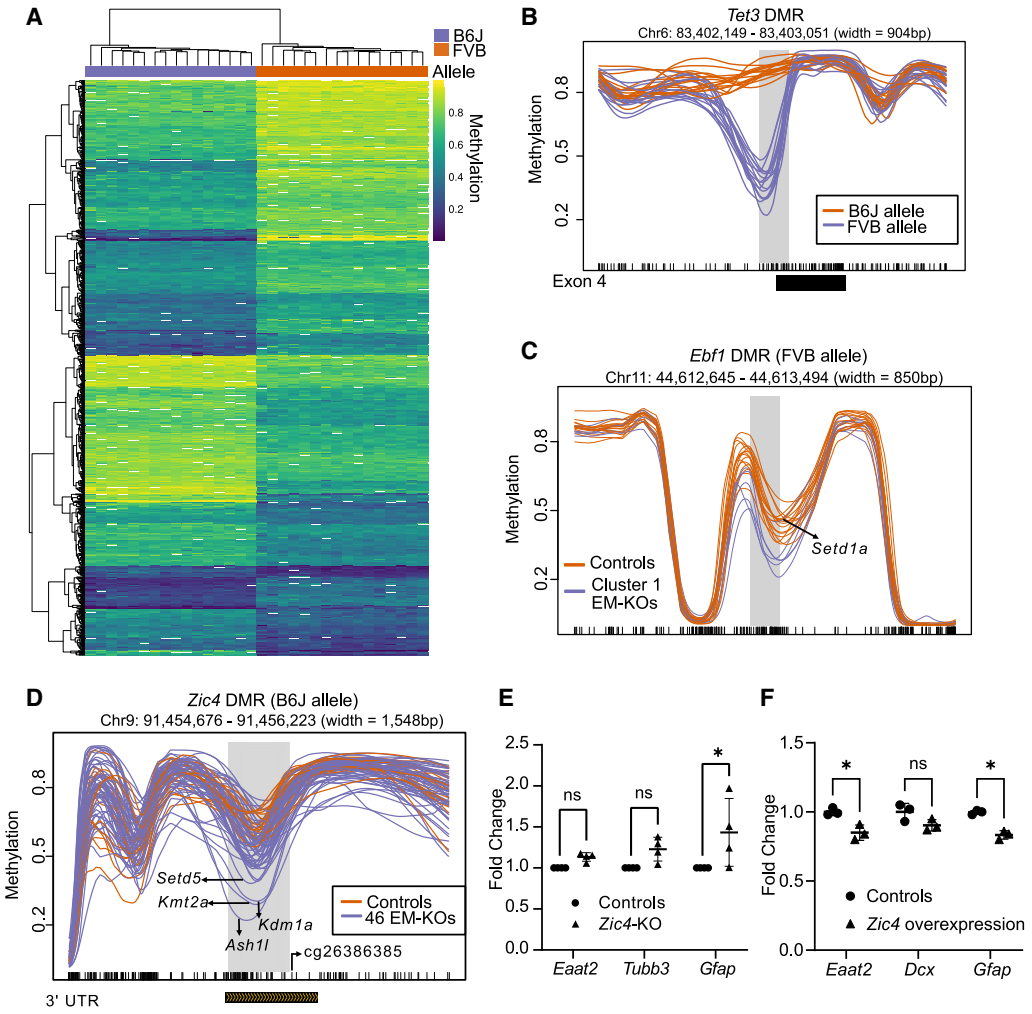


Figure 6. Haplotype-specific changes of DNAm. (*A*) Heatmap plot showing smoothed methylation of 1074 haplotype-specific DMRs across B6J and FVB haplotypes. Yellow and blue represent higher and lower DNAm, respectively. Each line in the *y*-axis represents a single DMR across haplotyped controls, and the *x*-axis represents haplotyped controls. (*B*) Haplotype-specific DMR in the *Tet3* gene. (*C*) Line plot showing a DMR in 5′ UTR of *Ebf1* between the FVB allele of control mNPC (orange) and the FVB allele of cluster 1 EM-KOs (purple). The DMR is highlighted in gray. Flanking regions of DMR are ±5 kb. On the *x*-axis, each tick mark represents a CpG in the mouse genome. (*D*) Line plot showing a DMR in 3′ UTR of *Zic4* between the B6J allele of control mNPC (orange) and the B6J allele of 46 EM-KOs (purple). The DMR is highlighted in gray. Flanking regions of DMR are ±5 kb. On the *x*-axis, each tick mark represents a CpG in the mouse genome. (*E*,*F*) qPCR results showing relative mRNA levels of *Eaat2*, *Dcx*/*Tubb3*, and *Gfap* after *Zic4* knockout compared with scrambled controls (*E*) and MYC-tag ZIC4 overexpression (*F*), compared with MYC-tag-only controls. A one-way ANOVA with Dunnett's correction was used. (*) Adjusted *P*-value < 0.05, (ns) not significant.

value = 0.00197) at day 6 compared with day 0 mNPCs in our neurodevelopmental model (Supplemental Fig. S7F). To evaluate the functional role of *Zic4* in mNPCs, we generated *Zic4*-KO cells and observed a nonsignificant increase in TUBB3-positive cells (Supplemental Fig. S7G,H), accompanied by increased expression of glial marker, compared with the scrambled controls (Fig. 6E). These findings suggest that loss of *Zic4* promotes premature differentiation phenotype. In contrast, KO of *Gsx1*, which is associated with the unique DMR identified in *Kmt2a*-KO cells, did not result in a comparable increase in TUBB3-positive cells (Supplemental Fig. S7G,H) or in the expression of neuronal and glial markers (Supplemental Fig. S7I). This suggests that the phenotype observed after *Zic4*-KO is unlikely to reflect a nonspecific response to the KO strategy and may instead represent a locus-specific effect. We also overexpressed MYC-tagged ZIC4 in mNPCs and compared with the MYC-tag alone. *Zic4* overexpression was associated with reduced expression of glial maturation markers (Fig. 6F; Supplemental Fig. S7J), suggesting ZIC4 may contribute to the maintenance of the NPC state and raising the possibility that it may act as a brake on neuronal maturation.

Discussion

Our study presents a comprehensive investigation into how EM disruption affects DNAm and gene expression in a disease-relevant neuronal system, offering insights into the presence and functional impact of DNAm changes beyond peripheral blood. By combining a mNPC model with ONT sequencing, haplotype phasing, and transcriptome profiling, we characterized the functional consequences of 46 EM gene KOs. Disruption of *Dnmt1* leads, as expected, to extensive changes in DNAm. A PCA of genome-wide DNAm suggests that the second largest effect on DNAm is from *Dnmt3b*

Downloaded from genome.cshlp.org on November 17, 2026 . Published by Cold Spring Harbor Laboratory Press

and *Kat6a*, although further investigation is required to assess these changes genome-wide. Because we aimed to identify DNAm changes that were likely to be causative rather than a consequence of the disease phenotype, we isolated and profiled the methylation levels relatively soon after KO (4 days). However, across the 46 EM-KOs, we observed little to no shared changes in DNAm and little evidence for KO-specific changes with the exception of a few KOs such as *Dnmt1* and *Dnmt3b*. This does not exclude the possibility that DNAm changes could occur at a later time point. Our data suggest that multiple TFs such as GSX1, MYC, and members of the SP and the E2F families may mediate or interpret EM-related epigenetic disruption. For instance, *Gsx1* was differentially expressed in *Kmt2a*-deficient cells, and many predicted *Gsx1* target genes were dysregulated in both *Kmt2a*-KO and *Dnmt1*-KO cells. Similarly, MYC and SP- and E2F-family binding motifs were enriched in promoters of shared DEGs, and GSEA showed significantly negative enrichment of MYC target genes. MYC, SP1, and E2F6 specifically are known binding partners of both KMT2A and DNMT1. These findings point to a model in which the EM indirectly modulates transcriptional networks through TFs, either via alteration of chromatin at TF binding sites or via interactions with the TFs themselves. Cross talk between histone modifications and DNAm is well documented. For example, H3K4 methylation blocks access of the de novo DNAm machinery, linking the histone methylation state to DNAm targeting (Ooi et al. 2007). Consistent with this idea, our clustering of promoter DNAm suggests that, at least in some EM-KO contexts, physical interactions with the DNAm machinery may play a role. Importantly, some TFs such as EGR1 are known to recruit TET1, further linking transcriptional networks to active DNA demethylation pathways (Sun et al. 2019).

We identified a hypomethylated DMR in the 3′ UTR of *Zic4*, which was shared across all 46 EM-KOs in one of the two haplotypes. This gene has been implicated in both murine and human neurodevelopment, and altered DNAm at this gene locus has been reported in peripheral blood from individuals with Sotos syndrome, a neurodevelopmental disorder caused by mutations in the epigenetic regulator *NSD1* (Choufani et al. 2015). However, the methylation changes are modest, and this gene is not differentially expressed in our EM-KOs. Nevertheless, *Zic4* is downregulated during differentiation, and overexpression of *Zic4* reduced expression of markers for glial differentiation (Fig. 6F; Supplemental Fig. S7F), suggesting that it may play a role in maintaining the NPC state. It remains unclear whether this gene contributes to the phenotypic overlap observed across MDEMs, but it could nevertheless have potential utility as a biomarker.

We have established a premature differentiation phenotype arising because of either *Dnmt1*-KO or *Kmt2a*-KO, consistent with observations across several other EM factors. In KMT2A-deficient mice, we previously found neuronal enhancers showed premature H3K4me1 enrichment in undifferentiated NPCs (Reynisdottir et al. 2025), and the same phenotype has been reported in two other disease-relevant contexts for Kabuki syndrome (Carosso et al. 2019; Fahrner et al. 2019). Moreover, studies of Kabuki syndrome neurons from a mouse model have shown an overrepresentation of aging-related loci (Boukas et al. 2024), further suggesting that premature differentiation may represent a unifying phenotype across a subset of MDEMs. In our NMF analysis, KMT2A and DNMT1 clustered with EZH2, KDM6A, and CREBBP, all of which have been shown to regulate neuronal stem cell maintenance and differentiation (Pereira et al. 2010; Wang et al. 2010; Lei and Jiao 2018). Genes associated with the latent factor of this group were enriched for functions relating to neuronal differentiation (Fig. 5B). This could suggest that even though the DNAm changes are very small, the disruption of these EM factors affects a core NPC gene network.

Despite the modest DNAm changes, we observed an impressive convergence of transcriptional dysregulation between *Dnmt1*- and *Kmt2a*-KOs, along with the premature differentiation phenotype. By comparing this to transcriptional changes during normal neuronal differentiation, we conclude that part of the overlap is secondary to the premature differentiation. Nonetheless, the overlap between the two KOs appears stronger (larger OR) than either overlap with normal differentiation, and the lack of methylation changes in *Kmt2a*-KOs indicates that expression changes are not a direct consequence of DNAm changes.

Although *Myc* transcript levels were unchanged, both KMT2A and DNMT1 are known MYC interactors (Kalkat et al. 2018), and we observed consistent downregulation of MYC target genes in the expected direction (Fig. 3E,F). This pattern strongly suggests reduced MYC activity. As MYC is a master cell-cycle regulator (Dong et al. 2014; García-Gutiérrez et al. 2019), either the loss of interaction with DNMT1 or KMT2A or the downregulation of its deubiquitinator USP28 (Popov et al. 2007) might be a critical factor contributing to the premature cell-cycle exit and neuronal differentiation phenotypes we observe. Further work is required to understand how the shared expression changes arise and especially to identify which epigenetic changes, if any, are causal in this context. Furthermore, the differentiation state should be carefully considered when analyzing gene expression, because premature or altered differentiation can be a major source of the observed changes and thus a confounder of such studies.

Together, our findings provide a framework for understanding how epigenetic machinery genes shape neurodevelopmental regulatory programs in disease-relevant cells. We identified transcription factors that may mediate specific chromatin and transcriptional consequences of EM disruption, while also recognizing that some TF-associated changes may reflect secondary cell-state changes. By leveraging long-read ONT sequencing for haplotype-aware DNAm analysis, our study further highlights the substantial contribution of strain-specific genetic variation to local methylation patterns. More broadly, this work establishes an integrated approach combining long-read methylation profiling, haplotype phasing, and transcriptomic analysis to investigate how epigenetic regulators contribute to neurodevelopment and to the molecular etiology of MDEMs.

Methods

Animals

B6J.129(Cg)-Gt(ROSA)26Sortm1.1(CAG-cas9*,-EGFP)Fezh/J(Strain 026179) (B6J) and FVB.129(B6)-Gt(ROSA)26Sortm1.1(CAG-cas9*, -EGFP)Fezh/J(Strain026558) (FVB) mice, each carrying a heterozygous Cas9 transgene, were obtained from Jackson Laboratory. Mice were bred within their respective background to generate homozygous Cas9-expressing offspring. Cas9 cassette integration was confirmed by PCR from ear clips using primers provided by Jackson Laboratory (Supplemental Table S14). All mice were kept on a 12-h/12-h dark–light cycle at room temperature (21°C–23°C) with ad libitum diet and water. Mouse importation and experimental protocols were in accordance with the Icelandic Food and Veterinary Authority (license no. 2208602) and approved by the National Expert Advisory Board on Animal Welfare.

Downloaded from genome.cshlp.org on November 17, 2026 . Published by Cold Spring Harbor Laboratory Press

Guide RNA design and isolation of plasmids

CRISPR-Cas9 sgRNAs were designed with an online tool (Labun et al. 2019; https://chopchop.cbu.uib.no/). Two sgRNAs, with the highest predicted efficiency and minimal mismatches per gene, were selected to ensure out-of-frame upon Cas9-mediated cleavage. All sgRNAs were verified with BLAT to ensure that none target any other sequences in either of the two genomes. Eight scrambled control sgRNA pairs (random sequence not binding in the murine genome) were designed as controls. Lentiviral CRISPR vectors (Replogle et al. 2020), each including one pair of sgRNAs (Supplemental Table S1) were synthesized by VectorBuilder. Bacterial stabs were streaked onto LB plates and plasmids isolated using ZymoPURE II plasmid Midiprep kit (Zymo D4201) and stored at −20°C until needed. All 56 dual-guide RNA lentiviral plasmids were Sanger sequenced to confirm the presence of the correct sgRNA pairs.

Dissections and primary NPCs isolation

The NPCs were isolated from F_1 hybrids of homozygous Cas9 mice (B6J and FVB). The isolation procedure was based on published protocols (Bernas et al. 2017; Rybachuk et al. 2019) with minor modifications (for details, see Supplemental Methods). NPCs were grown in neuronal growth medium (NGM), which included neurobasal medium supplemented with 1% B27 supplement (Thermo Fisher Scientific 17504044), 1% GlutaMAX (Thermo Fisher Scientific 35050061), 0.25% penicillin–streptomycin (Thermo Fisher Scientific 15140122) 20 ng/mL EGF (PeproTech AF-100-15), 20 ng/mL FGF2 (PeproTech 100-18B), and 2 µg/mL Heparin (MP Biomedicals 0210193125) on PDL/laminin-coated 6-well plates, and frozen down in NGM + 10% DMSO (Santa Cruz sc-358801).

Neuronal progenitor differentiation

NPCs (passage 3–4) were differentiated into mixed neuronal cultures by collecting them as previously described, counting and seeding 150,000 cells/well on a PDL/laminin-coated 24-well plate in 0.5 mL N2-neuronal induction medium (N2NIM) consisting of Neurobasal plus medium (Thermo Fisher Scientific A3582901) with 1× B-27 plus supplement (Thermo Fisher Scientific A3582801), 1× CultureOne supplement (Thermo Fisher Scientific A3320201), 1× N2 supplement (Thermo Fisher Scientific 17502048), 0.25× penicillin–streptomycin, and 0.25× GlutaMAX. This was supplemented with 20 ng/mL FGF2 and 10 ng/mL BDNF (Peprotech 450-02). On days 2 and 4, the medium was changed to N2NIM supplemented with 10 ng/mL FGF2, 10 ng/mL BDNF, and 10 ng/mL GDNF (ORF Genetics IK0900). At day 2 and day 6 of differentiation, neuronal cultures were collected and DNA and RNA isolated as described below.

Cell culture

For virus production, HEK293T cells were cultured in culturing media, DMEM/F12 supplemented with GlutaMAX (Thermo Fisher Scientific 31331093), and 10% fetal bovine serum (FBS; Thermo Fisher Scientific 10270106). All cells were incubated at 37°C with 5% CO_2. HEK293T cells were frozen down in culture media supplemented with 10% DMSO.

Virus production and transduction into NPCs

Lentivirus was produced in HEK293T cells and concentrated using a 4× lentivirus concentrator solution following a MD Anderson Cancer Center Functional Genomics Core protocol (Lo and Yee 2007; Kutner et al. 2009). Viral aliquots were stored at −80°C until use. Transduction efficiency was determined by fluorescence-activated cell sorting (FACS) of BFP-positive NPCs 48 h after transduction, and a transduction efficiency of ∼30% was used for all experiments. For details, see Supplemental Methods.

EM-KO in NPCs and validation

For EM-KO experiments, 250,000–300,000 NPCs were seeded on a 6-well plate 24 h prior to transduction. Cells were transduced with lentivirus in the presence of 8 µg/mL polybrene. Each lentivirus targeted a single EM gene, and nontargeting controls were used as negative controls for viral infection and culturing effects. After 24 h, cells were split and selected by 0.5 µg/mL puromycin (Thermo Fisher Scientific A1113802) for 2 days. Cells surviving puromycin treatment were cultured for another day without puromycin to allow them to recover and then harvested for experiments using Accutase as described above. Timing was selected based on the fact that average protein half-life in mouse primary neurons is ∼86 h (Mathieson et al. 2018), and for EM proteins, it is considered even less (∼40 h); thus, most of the EM proteins would be expected to be degraded at the time of our evaluation. The KO efficiency was determined by PCR, WB, and IF staining.

RNA isolation, cDNA synthesis, and real-time quantitative PCR

Cultured cells were harvested and lysed in TRIzol reagent (Thermo Fisher Scientific 15596018). Total RNA was isolated using a Direct-zol RNA microprep kit (Zymo Research R2062) based on the manufacturer's protocol. The concentration and quality of RNA were evaluated with NanoDrop (Thermo Fisher Scientific). One microgram of total RNA was used for cDNA synthesis with a high-capacity cDNA reverse transcription kit (Thermo Fisher Scientific 4368814). Real-time quantitative PCR (RT-qPCR) reactions were performed using Luna universal qPCR master mix (NEB M3003) and a CFX384 Touch real-time PCR detection system (Bio-Rad) according to manufacturer's protocol. Any primers used are provided in Supplemental Table S14.

Protein isolation and WB

NPCs were collected and lysed as described in the Supplemental Methods. WB was performed as has previously been described (Mahmood and Yang 2012), in which 15–25 µg of protein was loaded per sample and blotted onto PVDF membrane (Thermo Fisher Scientific 88520). Primary and secondary antibodies are listed in the Supplemental Methods and Supplemental Table S15.. Blots were visualized with Odyssey CLx Imager and protein quantification was evaluated by Image J (Schindelin et al. 2012).

Immunofluorescence

NPCs were cultured on PDL/laminin-coated 8-well culture slide (Falcon 354118) for 24–48 h, fixed with 4% paraformaldehyde (PFA), blocked with 5% NGS in 0.1% PBS-T, and stained using primary antibodies against rabbit anti-KMT2A, 1:200 (Cell Signaling 14197), rabbit anti-EAAT2 1:400 (Abcam ab41621), and mouse beta III tubulin 1:200 (Abcam ab78078), overnight. The following day, cells were stained using secondary antibodies: Alexa goat anti-rabbit 647, 1:1000 (Thermo Fisher Scientific A-21244) and Alexa goat antimouse 555, 1:1000 (Thermo Fisher Scientific A-32727). Cells were mounted with Fluoromount-G mounting medium, with DAPI (Thermo Fisher Scientific 00-4959-52). Images were captured with Olympus confocal microscopy (Olympus Fluoroview FV4000), processed with Fiji, and quantified with CellProfiler. Statistical analysis was done using GraphPad Prism v10.4.

Downloaded from genome.cshlp.org on November 17, 2026 . Published by Cold Spring Harbor Laboratory Press

Overexpression

NPCs were seeded at a density of 250,000–300,000 cells per well in PDL/laminin-coated 6-well plates 24 h prior to transfection. The following day, cells were cotransfected with 2.5 µg of either the MYC-tagged ZIC4 overexpression plasmid (Origene MR216949) or the corresponding MYC-alone plasmid backbone (control), along with 7.5 µL of Lipofectamine 3000, following the manufacturer's protocol. Cells were harvested 24 h posttransfection for downstream analysis.

DNA sample isolation and preparation

Genomic DNA isolated from cells using a Monarch HMW DNA extraction kit for cells and blood (NEB T3050) followed the manufacturer's protocol for DNA extraction from cells. The concentration and quality of DNA were measured by NanoDrop (Thermo Fisher Scientific) and Qubit to quantify the precise amount of double-stranded DNA via a Qubit dsDNA HS assay kit (Thermo Fisher Scientific Q33231). High-molecular-weight (HMW) DNA was sheared to 20–30 kb to achieve consistent size and to optimize ONT sequencing yield. HMW DNA was loaded to a hydro-tube assembled with a hydropore-syringe (Diagenode E07010003), inserted into the cassette, installed on a base unit, and then sheared by Megaruptor 3 (Diagenode) using the following settings: volume of 70 µL, speed of 30, and concentration of 50 ng/µL. The size of sheared DNA was evaluated with a HS large-fragment 50 kb kit (Agilent DNF-464-0500) on a Fragment Analyzer, proceeded by high-sensitivity large-fragment 50 kb analysis software.

ONT-DNA sequencing library construction

Library preparation for ONT-DNA sequencing used the ONT ligation sequencing kit V14 (ONT SQK-LSK114), using 1 µg sheared genomic HMW DNA in 47 µL nuclease-free water (Thermo Fisher Scientific Am9937) as input, followed by library preparing and loading on a R10.4.1 flow cell (FLO-PRO114M, ONT) on a PromethION 24 sequencer following the manufacturer's instructions (for details, see Supplemental Methods). Nanopore sequencing was performed using the following settings: run limit of 96 h, minimum read length of 200 bp, and superaccurate basecalling model with 5mC and 5hmC modified base context. To increase the output, flow cells were washed once after 22–24 h of sequencing using a Flow Cell Wash Kit XL (ONT EXP-WAS004-XL), followed by 1–1.5 h waiting time. Then priming and loading library procedures were the same as described previously. Around 70 Gb of estimated bases with an average read length of 20 kb were achieved per sample.

Detection of KO efficiency from ONT sequencing data

We developed a computational tool, samCRISPR, to estimate CRISPR-Cas9 KO efficiency using ONT long-read WGS data. The name "samCRISPR" references to both SAMtools, from which the mpileup format is used in KO efficiency calculations, and CRISPR-Cas9 genome editing technology. SAMtools is used to sort, index, and filter aligned reads and to generate mpileup output at the target site, which provides base-level resolution of read alignments. This output is parsed by our tool, samCRISPR, to identify substitutions, insertions, and deletions based on mpileup letter codes, allowing precise quantification of editing events and KO efficiency. The tool identifies sequencing reads that carry CRISPR-induced events within designated target regions using the mpileup output from SAMtools (Fig. 1F; Danecek et al. 2021). To eliminate the chance of counting sequencing errors in the vicinity of target regions as actual CRISPR events, the counting of CRISPR events was restricted to 1 bp upstream of and 1 bp downstream from Cas9 cut sites. CRISPR events were defined as mutations occurring within ±1 bp of the predicted cut site, located 3 bp upstream of the PAM sequence. This narrow window was chosen to minimize false positives caused by sequencing or alignment errors near Cas9 cleavage sites. KO efficiency was calculated as the ratio of reads with CRISPR events in the target region to the total number of reads mapped to that region. To validate samCRISPR results, KO efficiencies for selected EM-KOs were manually inspected using the Integrative Genomics Viewer (IGV) (Robinson et al. 2011). samCRISPR accepts a BAM file, a reference FASTA, or BED-formatted sgRNA coordinates as input and supports batch analysis of multiple BAM files and sgRNAs. It requires a Linux environment with SAMtools for mpileup generation and an R computing environment for calculating Wilson score confidence intervals (Agresti and Coull 1998).

Phasing of ONT data and obtaining CpG-level methylation data

We utilized a custom graph genome-based approach, a pipeline for long-read allele-specific methylation analysis (termed PLASMA), to integrate both FVB and B6 genomic sequences into a unified nonlinear reference coordinate suitable for allele-specific methylation analysis with minimal introduction of reference bias (Davidovich et al. 2026). A genome graph, a structure composed of nodes and edges, captures alternative alleles, structural variants, and indels across multiple genomes (Liao et al. 2023; Zhang et al. 2025). Unlike linear references, genome graphs support the simultaneous representation of multiple haplotypes, making them particularly suited for admixed or hybrid genomes.

The whole-genome alignment between the FVB and B6J reference genomes was performed using MUMmer4 v4.0 (Marçais et al. 2018) to identify heterozygous variants. Next, Jellyfish (Marçais and Kingsford 2011) was used to enumerate all 45-mers in each genome, which were subsequently classified into conserved nodes and variant edges. Edges <3 kb were aligned between genomes to derive CIGAR strings, enabling base-level coordinate conversion. From these, a pseudohybrid intermediate genome was constructed by selecting the longer edge between B6 and FVB, thus forming a unified coordinate system encompassing diversity of both strains.

Guppy v6.5.7 in MinKNOW software v23.04.5 was used to call canonical and modified bases (5mC, 5hmC) from raw current signal files FAST5/POD5. Reads were then aligned to both references using minimap2 v2.26 (retaining only high-confidence alignments (MAPQ > 20) (Li 2018). Strain-specific SNPs and alignment scores were used to assign reads to B6 or FVB haplotypes using WhatsHap v2.8 (Patterson et al. 2015). Methylation of each CpG was calculated using modkit v0.1.2 (https://github.com/nanoporetech/modkit). Importantly, all DNAm data were projected onto the pseudohybrid coordinate system, minimizing reference bias during haplotype-specific methylation analysis and allowing for a systematic comparison of methylation data from distinct reference coordinate systems.

Identification of DMRs

Methylation levels of each CpG for each sample were extracted from bedMethyl files generated by modkit, which contain per-CpG entries detailing genomic coordinates and read counts. Each file included about 21 million CpG sites. These data sets were imported into R to create BSseq objects (Hansen et al. 2012) for downstream DMR analysis. To ensure data reliability, unphased data sets retained only CpGs with ≥3× coverage in at least 80% of samples. For phased data, in which coverage was inherently lower, CpGs with ≥1× coverage across all samples were

Downloaded from genome.cshlp.org on November 17, 2026 . Published by Cold Spring Harbor Laboratory Press

included. DMRs were identified in phased data using the bsseq 1.39.4 (Hansen et al. 2012) and unphased data using dmrseq 1.22.1 (Korthauer et al. 2019) R packages. Dmrseq controls the false-discovery rate (FDR) whereas bsseq controls the FWER. For the phased data, smoothing was performed separately for each allele. Strain-specific CpGs were included during smoothing but were removed prior to DMR identification, following previous work (Wulfridge et al. 2019). This strategy enhances statistical power while reducing spurious DMR detection owing to strain-specific sequence differences. DMRs were filtered using the following criteria phased analysis: three or more CpGs per region, >5% mean methylation difference, and inverse CpG density ≤ 300 (defined as the region's genomic width divided by the number of CpGs). Criteria for unphased analysis was five or more CpGs and inverse CpG density ≤ 120.

Annotation of DMRs

We used annotatePeaks.pl program to annotate DMRs by using UCSC GRCm38 (mm10) mouse reference FASTA and UCSC mm10 refGene GTF files. That program calls a separate program, assignGenomeAnnotation, to efficiently assign DMRs to possible annotations genome wide. By default, in the case that some annotations overlap, HOMER assigns a priority based on the following: transcription start site (TSS; by default defined from −1 kb to +100 bp), TTS (by default defined from −100 bp to +1 kb), CDS exons, 5′ UTR exons, 3′ UTR exons, introns, and intergenic. Intergenic regions were considered either upstream (TSS) of or downstream (TTS) from genes.

To annotate DMRs in phased data, a custom pipeline was employed: The UCSC mm10 GTF file was converted to BED format using a Bash script. A Python script mapped coordinates between the mm10 genome and the pseudohybrid intermediate genome. This allowed accurate functional annotation of DMRs in a unified coordinate space representing both B6 and FVB haplotypes.

Enrichment analysis of DMRs in genomic features

Canonical transcripts of protein-coding genes in *Mus musculus* were downloaded from Ensembl using the biomaRt package v2.58.2 (Durinck et al. 2005) and annotated using GenomicFeatures package v1.54.4 (Lawrence et al. 2013) in conjunction with the UCSC genome annotation TxDb.Mmusculus.UCSC.mm10.knownGene v3.10.0. A subset of these genomic features was then selected to include only the canonical protein-coding transcripts. For CpG enrichment, we used the R computing environment to construct a 2 × 2 contingency table with the number of CpGs for each genomic feature and DMRs. A Fisher's exact test was used to assess the significance of enrichment.

DNAm overlap across individual data sets

An R-based pipeline was developed to visualize DMRs between mNPCs and day 6 neurons, incorporating additional conditions including *Dnmt1*-KO and *Kmt2a*-KOs and day 2 neurons. Unphased DMR coordinates (from mNPC vs. day 6 comparisons) were used to extract methylation data from the two experiments. CpGs with zero coverage in any sample were excluded. The remaining CpGs were smoothed with the *BSmooth()* function from the bsseq v1.39.4 package. The *normalizeToMatrix()* function from the EnrichedHeatmap v1.32 package was then used to map smoothed average methylation values from each group to a fixed-width matrix centered on the extended DMR intervals (±5 kb) with a 100 bp bin size, and heatmaps were generated using the same package.

PCA plot of genome-wide DNAm

To assess global DNAm variation, the mouse genome was segmented into 1 kb nonoverlapping tiles using the *tileGenome()* function from the GenomicRanges R package. Tiles containing more than two CpGs were retained, resulting in about 2.7 million genomic tiles. A custom R function was used to generate a PCA plot based on raw genome-wide DNAm levels across samples.

RNA isolation and sequencing

RNA was isolated as before using TRI Reagent and purified using a ZYMO Direct-zol RNA microprep kit. RNA concentration was measured using Qubit with the Qubit RNA HS assay kit (Thermo Fisher Scientific Q32852), and RNA integrity was assessed with a Bioanalyzer using a Agilent RNA 6000 nano kit (Agilent 5067-1511) according to the manufacturer's instructions. For *Kmt2a*-KOs and *Dnmt1*-KOs, the two genes were knocked out individually, together with a scrambled control, in four biological replicates each; RNA-isolated; and sent to Novogene Europe for mRNA Illumina sequencing. For WT neurodevelopmental cells, three biological replicates were isolated for each timepoint, RNA-extracted, and purified as before, and 200 ng total RNA from each sample was processed using the ONT PCR-cDNA barcoding kit (ONT SQK-PCB111.24), according to the manufacturer's instructions (version v111-revG). Samples were barcoded and pooled at equimolar ratios and then loaded onto 3× R9.4.1 flow-cells (FLO-PRO002) and sequenced on a PromethION 24 instrument.

Obtaining promoter coordinates of mouse protein-coding genes for NMF analysis

The *promoters()* function of the R package TxDb.Mmusculus.UCSC.mm10.knownGene v3.2 was utilized to identify UCSC mm10 coordinates of promoters. The promoter definition was considered 2 kb upstream of and 500 bp downstream from the TSS of the canonical transcript of each gene. The mouse protein coding gene list was downloaded from https://ftp.ncbi.nih.gov/gene/DATA/gene_info.gz.

Clustering of EM-KOs by NMF based on promoter DNAm abnormalities

We used NMF on smoothed DNAm levels of promoters of protein-coding genes (Cemgil 2009). CpGs with more than 3× coverage across at least >80% of samples were kept in our analysis. Any promoters with no retained CpGs were discarded. The number of latent factors (parameter k) was chosen to be three based on diagnostic plots of NMF and PPI interactions of EM components. The brunet model in the R package nmf v0.28 was employed in decomposition.

Computational and statistical analyses

Details of RNA sequencing analysis, TF motif enrichment analysis (background in Supplemental Table S16), protein–protein interaction, Gene Ontology, and GSEAs are described in Supplemental Methods.

Data visualization

For scatter plots and volcano plots, the R package ggplot2 was used (Wickham 2016). For Venn diagrams, the R package VennDiagram was used (Chen and Boutros 2011). The heatmaps were generated through the *pheatmap()* function of the R package pheatmap. R-based analyses were performed in R (R Core Team 2022). For individual gene expression values from RNA sequencing data and for

Downloaded from genome.cshlp.org on November 17, 2026 . Published by Cold Spring Harbor Laboratory Press

quantification results from qPCR, WB, and IF experiments, Graphpad Prism (v10.4) was used. Schematic figures were generated using BioRender (https://www.biorender.com), and figures were assembled into panels using Affinity Designer.

Code availability

Source code for samCRISPR is available at GitHub (https://github.com/kaanokay/samCRISPR) and provided as Supplemental Code 1. Other source codes are available at GitHub (https://github.com/kaanokay/DNA-methylation-paper) and provided as Supplemental Code 2.

Data access

All raw and processed sequencing data generated in this study have been submitted to the NCBI Gene Expression Omnibus (GEO; https://www.ncbi.nlm.nih.gov/geo/). Illumina short-read RNA sequencing data of *Kmt2a* and *Dnmt1* KO mNPCs are accessible under accession number GSE308011. ONT long-read RNA sequencing data of murine neurodevelopmental samples are accessible under accession number GSE308012. ONT long-read WGS data of murine neurodevelopmental samples are accessible under accession number GSE308528. EM-KO data are accessible under two accession numbers GSE308573 and GSE308669.

Competing interest statement

H.T.B. is a consultant for Mahzi Therapeutics and founder of KALDUR Therapeutics.

Acknowledgments

We thank Elvar Örn Jónsson and Þorgils Árni Hjálmarsson for their dedication and valuable efforts in troubleshooting data storage and analysis issues within the high-performance computing (HPC) cluster at the University of Iceland. We thank Olafur Th. Magnusson for advice regarding ONT sequencing and Þóra Dagbjartsdóttir for suggestions regarding mouse husbandry. H.T.B. has a grant from RANNIS (grant of excellence 217988-051) specifically covering this project. J.O. has a grant from Eimskipasjóður Íslands (doctoral grant 1238113). K.M. has a grant from RANNIS (postdoctoral fellowship 2410204-052). This work benefited from equipment from the SAMSNID infrastructure project, which brought the PromethION instrument to Iceland, and the IREI infrastructure project, which supports the high-performance computer cluster at the University of Iceland. We used ChatGPT (https://chatgpt.com/) to assist in improving scripting efficiency and robustness.

Author contributions: H.T.B. and K.D.H. conceptualized the project and supervised students. H.T.B. received the project funding. J.O., K.M., K.W., S.P., and T.P. performed experiments. K.O., K.M., K.D.H., J.O., S.P., A.D., and A.A. analyzed the data. H.T.B., K.D.H., K.M., J.O., and K.O. wrote the manuscript. K.J.A., K.W., S.P., T.P., and A.D. edited the manuscript.

References

Agresti A, Coull BA. 1998. Approximate is better than "exact" for interval estimation of binomial proportions. *Am Stat* **52:** 119–126. doi:10.1080/00031305.1998.10480550

Aref-Eshghi E, Rodenhiser DI, Schenkel LC, Lin H, Skinner C, Ainsworth P, Paré G, Hood RL, Bulman DE, Kernohan KD, et al. 2018. Genomic DNA methylation signatures enable concurrent diagnosis and clinical genetic variant classification in neurodevelopmental syndromes. *Am J Hum Genet* **102:** 156–174. doi:10.1016/j.ajhg.2017.12.008

Aref-Eshghi E, Kerkhof J, Pedro VP, Groupe DIF, Barat-Houari M, Ruiz-Pallares N, Andrau JC, Lacombe D, Van-Gils J, Fergelot P, et al. 2020. Evaluation of DNA methylation episignatures for diagnosis and phenotype correlations in 42 Mendelian neurodevelopmental disorders. *Am J Hum Genet* **106:** 356–370. doi:10.1016/j.ajhg.2020.01.019

Astorkia M, Liu Y, Pedrosa EM, Lachman HM, Zheng D. 2024. Molecular and network disruptions in neurodevelopment uncovered by single cell transcriptomics analysis of CHD8 heterozygous cerebral organoids. *Heliyon* **10:** e34862. doi:10.1016/j.heliyon.2024.e34862

Bachmann S, Linde J, Bell M, Spehr M, Zempel H, Zimmer-Bensch G. 2021. DNA methyltransferase 1 (DNMT1) shapes neuronal activity of human iPSC-derived glutamatergic cortical neurons. *Int J Mol Sci* **22:** 2034. doi:10.3390/ijms22042034

Bernas SN, Leiter O, Walker TL, Kempermann G. 2017. Isolation, culture and differentiation of adult hippocampal precursor cells. *Bio Protoc* **7:** e2603. doi:10.21769/BioProtoc.2603

Bjornsson HT. 2015. The mendelian disorders of the epigenetic machinery. *Genome Res* **25:** 1473–1481. doi:10.1101/gr.190629.115

Boukas L, Havrilla JM, Hickey PF, Quinlan AR, Bjornsson HT, Hansen KD. 2019. Coexpression patterns define epigenetic regulators associated with neurological dysfunction. *Genome Res* **29:** 532–542. doi:10.1101/gr.239442.118

Boukas L, Luperchio TR, Razi A, Hansen KD, Bjornsson HT. 2024. Neuron-specific chromatin disruption at CpG islands and aging-related regions in Kabuki syndrome mice. *Genome Res* **34:** 696–710. doi:10.1101/gr.278416.123

Bretones G, Delgado MD, León J. 2015. Myc and cell cycle control. *Biochim Biophys Acta* **1849:** 506–516. doi:10.1016/j.bbagrm.2014.03.013

Carosso GA, Boukas L, Augustin JJ, Nguyen HN, Winer BL, Cannon GH, Robertson JD, Zhang L, Hansen KD, Goff LA, et al. 2019. Precocious neuronal differentiation and disrupted oxygen responses in Kabuki syndrome. *JCI Insight* **4:** e129375. doi:10.1172/jci.insight.129375

Cemgil AT. 2009. Bayesian inference for nonnegative matrix factorisation models. *Comput Intell Neurosci* **2009:** 785152. doi:10.1155/2009/785152

Chen H, Boutros PC. 2011. VennDiagram: a package for the generation of highly-customizable Venn and Euler diagrams in R. *BMC Bioinformatics* **12:** 35. doi:10.1186/1471-2105-12-35

Choufani S, Cytrynbaum C, Chung BH, Turinsky AL, Grafodatskaya D, Chen YA, Cohen AS, Dupuis L, Butcher DT, Siu MT, et al. 2015. NSD1 mutations generate a genome-wide DNA methylation signature. *Nat Commun* **6:** 10207. doi:10.1038/ncomms10207

Ciceri G, Baggiolini A, Cho HS, Kshirsagar M, Benito-Kwiecinski S, Walsh RM, Aromolaran KA, Gonzalez-Hernandez AJ, Munguba H, Koo SY, et al. 2024. An epigenetic barrier sets the timing of human neuronal maturation. *Nature* **626:** 881–890. doi:10.1038/s41586-023-06984-8

Ciptasari U, van Bokhoven H. 2020. The phenomenal epigenome in neurodevelopmental disorders. *Hum Mol Genet* **29:** R42–R50. doi:10.1093/hmg/ddaa175

Coltogirone RA, Sherfinski EI, Dobler ZA, Peterson SN, Andlinger AR, Fadel LC, Patrick RL, Bergeron SA. 2023. Gsx2, but not Gsx1, is necessary for early forebrain patterning and long-term survival in zebrafish. *Dev Dyn* **252:** 377–399. doi:10.1002/dvdy.542

Danecek P, Bonfield JK, Liddle J, Marshall J, Ohan V, Pollard MO, Whitwham A, Keane T, McCarthy SA, Davies RM, et al. 2021. Twelve years of SAMtools and BCFtools. *GigaScience* **10:** giab008. doi:10.1093/gigascience/giab008

Davidovich A, Cuomo D, Su H, Kambhampati S, Gong Q, Naron A, Tryggvadottir R, McMillan L, Hansen KD, Threadgill DW, et al. 2026. Non-mendelian inheritance of DNA methylation patterns in mice. *Nat Genet* **58:** 1409–1422. doi:10.1038/s41588-026-02604-z

Deaton AM, Bird A. 2011. CpG islands and the regulation of transcription. *Genes Dev* **25:** 1010–1022. doi:10.1101/gad.2037511

Do C, Lang CF, Lin J, Darbary H, Krupska I, Gaba A, Petukhova L, Vonsattel JP, Gallagher MP, Goland RS, et al. 2016. Mechanisms and disease associations of haplotype-dependent allele-specific DNA methylation. *Am J Hum Genet* **98:** 934–955. doi:10.1016/j.ajhg.2016.03.027

Dong P, Maddali MV, Srimani JK, Thélot F, Nevins JR, Mathey-Prevot B, You L. 2014. Division of labour between Myc and G1 cyclins in cell cycle commitment and pace control. *Nat Commun* **5:** 4750. doi:10.1038/ncomms5750

Durinck S, Moreau Y, Kasprzyk A, Davis S, De Moor B, Brazma A, Huber W. 2005. BioMart and Bioconductor: a powerful link between biological databases and microarray data analysis. *Bioinformatics* **21:** 3439–3440. doi:10.1093/bioinformatics/bti525

Fahrner JA, Lin WY, Riddle RC, Boukas L, DeLeon VB, Chopra S, Lad SE, Luperchio TR, Hansen KD, Bjornsson HT. 2019. Precocious chondrocyte differentiation disrupts skeletal growth in Kabuki syndrome mice. *JCI Insight* **4:** e129380. doi:10.1172/jci.insight.129380

Feng J, Zhou Y, Campbell SL, Le T, Li E, Sweatt JD, Silva AJ, Fan G. 2010. Dnmt1 and Dnmt3a maintain DNA methylation and regulate synaptic

Downloaded from genome.cshlp.org on November 17, 2026 . Published by Cold Spring Harbor Laboratory Press

function in adult forebrain neurons. *Nat Neurosci* **13:** 423–430. doi:10.1038/nn.2514
Feng W, Khan MA, Bellvis P, Zhu Z, Bernhardt O, Herold-Mende C, Liu HK. 2013. The chromatin remodeler CHD7 regulates adult neurogenesis via activation of SoxC transcription factors. *Cell Stem Cell* **13:** 62–72. doi:10.1016/j.stem.2013.05.002
Foroutan A, Haghshenas S, Bhai P, Levy MA, Kerkhof J, McConkey H, Niceta M, Ciolfi A, Pedace L, Miele E, et al. 2022. Clinical utility of a unique genome-wide DNA methylation signature for KMT2A-related syndrome. *Int J Mol Sci* **23:** 1815. doi:10.3390/ijms23031815
Friedrich G, Soriano P. 1991. Promoter traps in embryonic stem cells: a genetic screen to identify and mutate developmental genes in mice. *Genes Dev* **5:** 1513–1523. doi:10.1101/gad.5.9.1513
Fu MP, Merrill SM, Sharma M, Gibson WT, Turvey SE, Kobor MS. 2023. Rare diseases of epigenetic origin: challenges and opportunities. *Front Genet* **14:** 1113086. doi:10.3389/fgene.2023.1113086
García-Gutiérrez L, Bretones G, Molina E, Arechaga I, Symonds C, Acosta JC, Blanco R, Fernández A, Alonso L, Sicinski P, et al. 2019. Myc stimulates cell cycle progression through the activation of Cdk1 and phosphorylation of p27. *Sci Rep* **9:** 18693. doi:10.1038/s41598-019-54917-1
Garel S, Marín F, Grosschedl R, Charnay P. 1999. Ebf1 controls early cell differentiation in the embryonic striatum. *Development* **126:** 5285–5294. doi:10.1242/dev.126.23.5285
Gigante S, Gouil Q, Lucattini A, Keniry A, Beck T, Tinning M, Gordon L, Woodruff C, Speed TP, Blewitt ME, et al. 2019. Using long-read sequencing to detect imprinted DNA methylation. *Nucleic Acids Res* **47:** e46. doi:10.1093/nar/gkz107
Grinberg I, Northrup H, Ardinger H, Prasad C, Dobyns WB, Millen KJ. 2004. Heterozygous deletion of the linked genes *ZIC1* and *ZIC4* is involved in Dandy-Walker malformation. *Nat Genet* **36:** 1053–1055. doi:10.1038/ng1420
Hansen KD, Langmead B, Irizarry RA. 2012. BSmooth: from whole genome bisulfite sequencing reads to differentially methylated regions. *Genome Biol* **13:** R83. doi:10.1186/gb-2012-13-10-r83
Irion S, Luche H, Gadue P, Fehling HJ, Kennedy M, Keller G. 2007. Identification and targeting of the ROSA26 locus in human embryonic stem cells. *Nat Biotechnol* **25:** 1477–1482. doi:10.1038/nbt1362
Jain M, Olsen HE, Paten B, Akeson M. 2016. The Oxford Nanopore MinION: delivery of nanopore sequencing to the genomics community. *Genome Biol* **17:** 239. doi:10.1186/s13059-016-1103-0
Jakovcevski M, Ruan H, Shen EY, Dincer A, Javidfar B, Ma Q, Peter CJ, Cheung I, Mitchell AC, Jiang Y, et al. 2015. Neuronal Kmt2a/Mll1 histone methyltransferase is essential for prefrontal synaptic plasticity and working memory. *J Neurosci* **35:** 5097–5108. doi:10.1523/JNEUROSCI.3004-14.2015
Jönsson ME, Ludvik Brattås P, Gustafsson C, Petri R, Yudovich D, Pircs K, Verschuere S, Mådsen S, Hansson J, Larsson J, et al. 2019. Activation of neuronal genes via LINE-1 elements upon global DNA demethylation in human neural progenitors. *Nat Commun* **10:** 3182. doi:10.1038/s41467-019-11150-8
Kalkat M, Resetca D, Lourenco C, Chan P-K, Wei Y, Shiah Y-J, Vitkin N, Tong Y, Sunnerhagen M, Done SJ, et al. 2018. MYC protein interactome profiling reveals functionally distinct regions that cooperate to drive tumorigenesis. *Mol Cell* **72:** 836–848.e7. doi:10.1016/j.molcel.2018.09.031
Kerimoglu C, Sakib MS, Jain G, Benito E, Burkhardt S, Capece V, Kaurani L, Halder R, Agís-Balboa RC, Stilling R, et al. 2017. KMT2A and KMT2B mediate memory function by affecting distinct genomic regions. *Cell Rep* **20:** 538–548. doi:10.1016/j.celrep.2017.06.072
Kim J, Lu X, Stubbs L. 1999. *Zim1*, a maternally expressed mouse Kruppel-type zinc-finger gene located in proximal chromosome 7. *Hum Mol Genet* **8:** 847–854. doi:10.1093/hmg/8.5.847
Kim S, Kim H, Um JW. 2018. Synapse development organized by neuronal activity-regulated immediate-early genes. *Exp Mol Med* **50:** 1–7. doi:10.1038/s12276-018-0025-1
Kimura H, Shiota K. 2003. Methyl-CpG-binding protein, MeCP2, is a target molecule for maintenance DNA methyltransferase, Dnmt1. *J Biol Chem* **278:** 4806–4812. doi:10.1074/jbc.M209923200
Korthauer K, Chakraborty S, Benjamini Y, Irizarry RA. 2019. Detection and accurate false discovery rate control of differentially methylated regions from whole genome bisulfite sequencing. *Biostatistics* **20:** 367–383. doi:10.1093/biostatistics/kxy007
Kutner RH, Zhang XY, Reiser J. 2009. Production, concentration and titration of pseudotyped HIV-1-based lentiviral vectors. *Nat Protoc* **4:** 495–505. doi:10.1038/nprot.2009.22
Labun K, Montague TG, Krause M, Torres Cleuren YN, Tjeldnes H, Valen E. 2019. CHOPCHOP v3: expanding the CRISPR web toolbox beyond genome editing. *Nucleic Acids Res* **47:** W171–W174. doi:10.1093/nar/gkz365
La Manno G, Siletti K, Furlan A, Gyllborg D, Vinsland E, Mossi Albiach A, Mattsson Langseth C, Khven I, Lederer AR, Dratva LM, et al. 2021. Molecular architecture of the developing mouse brain. *Nature* **596:** 92–96. doi:10.1038/s41586-021-03775-x
Lawrence M, Huber W, Pagès H, Aboyoun P, Carlson M, Gentleman R, Morgan MT, Carey VJ. 2013. Software for computing and annotating genomic ranges. *PLoS Comput Biol* **9:** e1003118. doi:10.1371/journal.pcbi.1003118
Lei X, Jiao J. 2018. UTX affects neural stem cell proliferation and differentiation through PTEN signaling. *Stem Cell Reports* **10:** 1193–1207. doi:10.1016/j.stemcr.2018.02.008
Li H. 2018. Minimap2: pairwise alignment for nucleotide sequences. *Bioinformatics* **34:** 3094–3100. doi:10.1093/bioinformatics/bty191
Liang H, Xiao G, Yin H, Hippenmeyer S, Horowitz JM, Ghashghaei HT. 2013. Neural development is dependent on the function of specificity protein 2 in cell cycle progression. *Development* **140:** 552–561. doi:10.1242/dev.085621
Liao WW, Asri M, Ebler J, Doerr D, Haukness M, Hickey G, Lu S, Lucas JK, Monlong J, Abel HJ, et al. 2023. A draft human pangenome reference. *Nature* **617:** 312–324. doi:10.1038/s41586-023-05896-x
Lo HL, Yee JK. 2007. Production of vesicular stomatitis virus G glycoprotein (VSV-G) pseudotyped retroviral vectors. *Curr Protoc Hum Genet* **Chapter 12:** Unit 12.7. doi:10.1002/0471142905.hg1207s52
Luperchio TR, Boukas L, Zhang L, Pilarowski G, Jiang J, Kalinousky A, Hansen KD, Bjornsson HT. 2021. Leveraging the mendelian disorders of the epigenetic machinery to systematically map functional epigenetic variation. *eLife* **10:** e65884. doi:10.7554/eLife.65884
Mahmood T, Yang PC. 2012. Western blot: technique, theory, and trouble shooting. *N Am J Med Sci* **4:** 429–434. doi:10.4103/1947-2714.100998
Marçais G, Kingsford C. 2011. A fast, lock-free approach for efficient parallel counting of occurrences of *k*-mers. *Bioinformatics* **27:** 764–770. doi:10.1093/bioinformatics/btr011
Marçais G, Delcher AL, Phillippy AM, Coston R, Salzberg SL, Zimin A. 2018. MUMmer4: a fast and versatile genome alignment system. *PLoS Comput Biol* **14:** e1005944. doi:10.1371/journal.pcbi.1005944
Mathieson T, Franken H, Kosinski J, Kurzawa N, Zinn N, Sweetman G, Poeckel D, Ratnu VS, Schramm M, Becher I, et al. 2018. Systematic analysis of protein turnover in primary cells. *Nat Commun* **9:** 689. doi:10.1038/s41467-018-03106-1
Noguchi H, Kimura A, Murao N, Namihira M, Nakashima K. 2016. Prenatal deletion of *DNA methyltransferase 1* in neural stem cells impairs neurogenesis and causes anxiety-like behavior in adulthood. *Neurogenesis (Austin)* **3:** e1232679. doi:10.1080/23262133.2016.1232679
Ooi SK, Qiu C, Bernstein E, Li K, Jia D, Yang Z, Erdjument-Bromage H, Tempst P, Lin SP, Allis CD, et al. 2007. DNMT3L connects unmethylated lysine 4 of histone H3 to de novo methylation of DNA. *Nature* **448:** 714–717. doi:10.1038/nature05987
Oughtred R, Rust J, Chang C, Breitkreutz BJ, Stark C, Willems A, Boucher L, Leung G, Kolas N, Zhang F, et al. 2021. The BioGRID database: a comprehensive biomedical resource of curated protein, genetic, and chemical interactions. *Protein Sci* **30:** 187–200. doi:10.1002/pro.3978
Park DH, Hong SJ, Salinas RD, Liu SJ, Sun SW, Sgualdino J, Testa G, Matzuk MM, Iwamori N, Lim DA. 2014. Activation of neuronal gene expression by the JMJD3 demethylase is required for postnatal and adult brain neurogenesis. *Cell Rep* **8:** 1290–1299. doi:10.1016/j.celrep.2014.07.060
Patterson M, Marschall T, Pisanti N, van Iersel L, Stougie L, Klau GW, Schönhuth A. 2015. WhatsHap: weighted haplotype assembly for future-generation sequencing reads. *J Comput Biol* **22:** 498–509. doi:10.1089/cmb.2014.0157
Pei Z, Wang B, Chen G, Nagao M, Nakafuku M, Campbell K. 2011. Homeobox genes *Gsx1* and *Gsx2* differentially regulate telencephalic progenitor maturation. *Proc Natl Acad Sci* **108:** 1675–1680. doi:10.1073/pnas.1008824108
Pereira JD, Sansom SN, Smith J, Dobenecker MW, Tarakhovsky A, Livesey FJ. 2010. Ezh2, the histone methyltransferase of PRC2, regulates the balance between self-renewal and differentiation in the cerebral cortex. *Proc Natl Acad Sci* **107:** 15957–15962. doi:10.1073/pnas.1002530107
Persengiev SP, Kondova II, Kilpatrick DL. 1999. E2f4 actively promotes the initiation and maintenance of nerve growth factor-induced cell differentiation. *Mol Cell Biol* **19:** 6048–6056. doi:10.1128/MCB.19.9.6048
Pinello L, Canver MC, Hoban MD, Orkin SH, Kohn DB, Bauer DE, Yuan GC. 2016. Analyzing CRISPR genome-editing experiments with CRISPResso. *Nat Biotechnol* **34:** 695–697. doi:10.1038/nbt.3583
Plaisier CL, O'Brien S, Bernard B, Reynolds S, Simon Z, Toledo CM, Ding Y, Reiss DJ, Paddison PJ, Baliga NS. 2016. Causal mechanistic regulatory network for glioblastoma deciphered using systems genetics network analysis. *Cell Syst* **3:** 172–186. doi:10.1016/j.cels.2016.06.006
Popov N, Wanzel M, Madiredjo M, Zhang D, Beijersbergen R, Bernards R, Moll R, Elledge SJ, Eilers M. 2007. The ubiquitin-specific protease USP28 is required for MYC stability. *Nat Cell Biol* **9:** 765–774. doi:10.1038/ncb1601

Downloaded from genome.cshlp.org on November 17, 2026 . Published by Cold Spring Harbor Laboratory Press

R Core Team. 2022. *R: a language and environment for statistical computing*. R Foundation for Statistical Computing, Vienna. https://www.R-project.org/.

Replogle JM, Norman TM, Xu A, Hussmann JA, Chen J, Cogan JZ, Meer EJ, Terry JM, Riordan DP, Srinivas N, et al. 2020. Combinatorial single-cell CRISPR screens by direct guide RNA capture and targeted sequencing. *Nat Biotechnol* **38:** 954–961. doi:10.1038/s41587-020-0470-y

Reynisdottir T, Anderson KJ, Möller K, Pétursson S, Brinn A, Franklin KP, Ouyang J, Snorradottir AO, Lutz CM, Zuberi AR, et al. 2025. In utero rescue of neurological dysfunction in a mouse model of Wiedemann-Steiner syndrome. *JCI Insight* **10:** e187039. doi:10.1172/jci.insight.187039

Robinson JT, Thorvaldsdóttir H, Winckler W, Guttman M, Lander ES, Getz G, Mesirov JP. 2011. Integrative genomics viewer. *Nat Biotechnol* **29:** 24–26. doi:10.1038/nbt.1754

Rybachuk O, Kopach O, Pivneva T, Kyryk V. 2019. Isolation of neural stem cells from the embryonic mouse hippocampus for in vitro growth or engraftment into a host tissue. *Bio Protoc* **9:** e3165. doi:10.21769/BioProtoc.3165

Samara A, Spildrejorde M, Sharma A, Falck M, Leithaug M, Modafferi S, Bjornstad PM, Acharya G, Gervin K, Lyle R, et al. 2022. A multi-omics approach to visualize early neuronal differentiation from hESCs in 4D. *iScience* **25:** 105279. doi:10.1016/j.isci.2022.105279

Schindelin J, Arganda-Carreras I, Frise E, Kaynig V, Longair M, Pietzsch T, Preibisch S, Rueden C, Saalfeld S, Schmid B, et al. 2012. Fiji: an open-source platform for biological-image analysis. *Nat Methods* **9:** 676–682. doi:10.1038/nmeth.2019

Schoof M, Launspach M, Holdhof D, Nguyen L, Engel V, Filser S, Peters F, Immenschuh J, Hellwig M, Niesen J, et al. 2019. The transcriptional coactivator and histone acetyltransferase CBP regulates neural precursor cell development and migration. *Acta Neuropathol Commun* **7:** 199. doi:10.1186/s40478-019-0849-5

Sheu JR, Hsieh CY, Jayakumar T, Lin GY, Lee HN, Huang SW, Yang CH. 2019. HDAC6 dysfunction contributes to impaired maturation of adult neurogenesis in vivo: vital role on functional recovery after ischemic stroke. *J Biomed Sci* **26:** 27. doi:10.1186/s12929-019-0521-1

Sun Z, Xu X, He J, Murray A, Sun MA, Wei X, Wang X, McCoig E, Xie E, Jiang X, et al. 2019. EGR1 recruits TET1 to shape the brain methylome during development and upon neuronal activity. *Nat Commun* **10:** 3892. doi:10.1038/s41467-019-11905-3

Syal C, Seegobin M, Sarma SN, Gouveia A, Hsu K, Niibori Y, He L, Wondisford FE, Frankland PW, Wang J. 2018. Ectopic expression of aPKC-mediated phosphorylation in p300 modulates hippocampal neurogenesis, CREB binding and fear memory differently with age. *Sci Rep* **8:** 13489. doi:10.1038/s41598-018-31657-2

Tao C, Liu J, Li Z, Lai P, Zhang S, Qu J, Tang Y, Liu A, Zou Z, Bai X, et al. 2022. DNMT1 is a negative regulator of osteogenesis. *Biol Open* **11:** bio058534. doi:10.1242/bio.058534

Tycko B. 2010. Allele-specific DNA methylation: beyond imprinting. *Hum Mol Genet* **19:** R210–R220. doi:10.1093/hmg/ddq376

Veyrac A, Besnard A, Caboche J, Davis S, Laroche S. 2014. The transcription factor Zif268/Egr1, brain plasticity, and memory. *Prog Mol Biol Transl Sci* **122:** 89–129. doi:10.1016/B978-0-12-420170-5.00004-0

Villa CE, Cheroni C, Dotter CP, López-Tóbon A, Oliveira B, Sacco R, Yahya AC, Morandell J, Gabriele M, Tavakoli MR, et al. 2022. CHD8 haploinsufficiency links autism to transient alterations in excitatory and inhibitory trajectories. *Cell Rep* **39:** 110615. doi:10.1016/j.celrep.2022.110615

Wang J, Weaver IC, Gauthier-Fisher A, Wang H, He L, Yeomans J, Wondisford F, Kaplan DR, Miller FD. 2010. CBP histone acetyltransferase activity regulates embryonic neural differentiation in the normal and Rubinstein-Taybi syndrome brain. *Dev Cell* **18:** 114–125. doi:10.1016/j.devcel.2009.10.023

Wang S, Rhijn JV, Akkouh I, Kogo N, Maas N, Bleeck A, Ortiz IS, Lewerissa E, Wu KM, Schoenmaker C, et al. 2022. Loss-of-function variants in the schizophrenia risk gene SETD1A alter neuronal network activity in human neurons through the cAMP/PKA pathway. *Cell Rep* **39:** 110790. doi:10.1016/j.celrep.2022.110790

Wei Z, Zheng S, Spangler SA, Yu C, Hoogenraad CC, Zhang M. 2011. Liprin-mediated large signaling complex organization revealed by the liprin-alpha/CASK and liprin-alpha/liprin-beta complex structures. *Mol Cell* **43:** 586–598. doi:10.1016/j.molcel.2011.07.021

Wickham H. 2016. *ggplot2*. Springer-Verlag, New York.

Wulfridge P, Langmead B, Feinberg AP, Hansen KD. 2019. Analyzing whole genome bisulfite sequencing data from highly divergent genotypes. *Nucleic Acids Res* **47:** e117. doi:10.1093/nar/gkz674

You L, Yan K, Zou J, Zhao H, Bertos NR, Park M, Wang E, Yang XJ. 2015. The lysine acetyltransferase activator Brpf1 governs dentate gyrus development through neural stem cells and progenitors. *PLoS Genet* **11:** e1005034. doi:10.1371/journal.pgen.1005034

Zhang J, Ji F, Liu Y, Lei X, Li H, Ji G, Yuan Z, Jiao J. 2014. Ezh2 regulates adult hippocampal neurogenesis and memory. *J Neurosci* **34:** 5184–5199. doi:10.1523/JNEUROSCI.4129-13.2014

Zhang W, Macias-Velasco JF, Zhuo X, Belter EA Jr, Tomlinson C, Garza J, Tekkey N, Li D, Wang T. 2025. methylGrapher: genome-graph-based processing of DNA methylation data from whole genome bisulfite sequencing. *Nucleic Acids Res* **53:** gkaf028. doi:10.1093/nar/gkaf028

Zhou Q, Obana EA, Radomski KL, Sukumar G, Wynder C, Dalgard CL, Doughty ML. 2016. Inhibition of the histone demethylase Kdm5b promotes neurogenesis and derepresses *Reln* (reelin) in neural stem cells from the adult subventricular zone of mice. *Mol Biol Cell* **27:** 627–639. doi:10.1091/mbc.E15-07-0513

Received November 18, 2025; accepted in revised form October 6, 2026.